Oil & Natural Gas Technology

Detection and Production of Methane Hydrate

Semi-annual Progress Report

Reporting Period: November-March, 2010

Submitted by:
Rice University, University of Texas, and Oklahoma State University

George J. Hirasaki and Walter Chapman, Chemical and Biomolecular Engineering
Gerald R. Dickens, Colin A. Zelt, and Brandon E. Dugan, Earth Science
Kishore K. Mohanty, University of Texas
Priyank Jaiswal, Oklahoma State University

May, 2010

DOE Award No.: DE-FC26-06NT42960
John Terneus, Program Officer

Rice University – MS 362
6100 Main St.
Houston, TX 77251-1892
Phone: 713-348-5416; FAX: 713-348-5478; Email: gjh@rice.edu

Prepared for:
United States Department of Energy
National Energy Technology Laboratory

Office of Fossil Energy

Table of Contents

Disclaimer

Executive Summary

Task 5: Carbon Inputs and Outputs to Gas Hydrate Systems

Glen Snyder is presently assisting Andrew Hunt of the USGS Noble Gas laboratory in Colorado to develop sampling methods for determining noble gas isotopic composition of interstitial pore fluids and gas hydrate recovered from piston coring.

Task 6: Numerical Models for Quantification of Hydrate and Free Gas Accumulations

In Subtask 6.3, Compositional Effect on BSR, Synthetic Seismic Response, the ability to generate synthetic seismogram with Ricker wavelets on some cases of hydrate/gas transition has been established.

Subtask 6.4. Blanking and chaotic zones due to hydrate distribution. We have started working on acoustic velocity profiles in different types of sediment layers. Due to hydrate accumulation, the velocity in different types of sediment layers can become similar with each other.

Subtask 6.8 (b): Sulfate, bicarbonate, calcium and carbon isotope ($\delta^{13}C$) profiles as an indicator of methane flux above marine gas hydrate systems

Methane flux is an important constraint on the amount of hydrate that may be present in marine sediments. One approach to determine this flux is to use the depth to the sulfate-methane transition (SMT). Pore-water sulfate concentrations deplete to zero in shallow sediments above methane hydrate systems. Many authors attributed these chemical gradients to anaerobic oxidation of methane (AOM) at the SMT and directly related the depth of the SMT to the upward methane flux at steady-state conditions. However, an alternative mechanism for sulfate consumption by particulate organic carbon (POC) has been interpreted by various authors. To reconcile these two interpretations, *Bhatnagar and others'* 1D model (2008) was extended and methane, sulfate, dissolved inorganic carbon (DIC), calcium and carbon isotope concentration profiles were computed with both advective and diffusive fluxes.

Task 7: Analysis of Production Strategy

A large deposit of gas hydrate is found in the Gulf of Mexico (GOM) block AC 818. In the last 6 months, we have worked on assessing the production from this block using a thermal, compositional, 3-D simulator in equilibrium mode. Four components (water, methane, hydrate and salt) and four phases (gas, aqueous-phase, hydrate and ice) are considered where salt is assumed to be in aqueous phase only. The reservoir GOM, block AC 818 is reported to be an unconfined reservoir. For these types of reservoirs, depressurization is ineffective and warm water flooding is necessary for production. We study different well configurations for production from this hydrate reservoir using warm water flooding.

Task 8: Seafloor and Borehole Stability

We are concentrating on different scales of failure in gas hydrate systems ranging from bed-scale fracture genesis to regional-scale slope failure (Subtask 8.2). This work, which is grounded on data collected from previous hydrate studies (Subtasks 8.1 and 8.3), is not only providing constraints on what drives different types of failure, but it is also helping us characterize the controls on heterogeneous hydrate accumulations. This has led to our involvement in other hydrate collaborations with the Chevron Gulf of Mexico JIP, hydrate studies in China, and hydrate studies in Cascadia (building on Subtask 8.3 and general collaborations within DOE and outside of DOE).

Task 9: Geophysical Imaging of Gas Hydrate and Free Gas Accumulations

(This will be reported in End of Phase 4 Report)

Background

A. Objective

This project seeks to understand regional differences in gas hydrate systems from the perspective of as an energy resource, geohazard, and long-term climate influence. Specifically, the effort will: (1) collect data and conceptual models that targets causes of gas hydrate variance, (2) construct numerical models that explain and predict regional-scale gas hydrate differences in 2- and 3-dimensions with minimal "free parameters", (3) simulate hydrocarbon production from various gas hydrate systems to establish promising resource characteristics, (4) perturb different gas hydrate systems to assess potential impacts of hot fluids on seafloor stability and well stability, and (5) develop geophysical approaches that enable remote quantification of gas hydrate heterogeneities so that they can be characterized with minimal costly drilling. Our integrated program takes advantage of the fact that we have a close working team comprised of experts in distinct disciplines.

The expected outcomes of this project are improved exploration and production technology for production of natural gas from methane hydrates and improved safety through understanding of seafloor and well bore stability in the presence of hydrates.

B. Scope of Work

The scope of this project is to more fully characterize, understand, and appreciate fundamental differences in the amount and distribution of gas hydrate and how this affects the production potential of a hydrate accumulation in the marine environment. The effort will combine existing information from locations in the ocean that are dominated by low permeability sediments with small amounts of high permeability sediments, one permafrost location where extensive hydrates exist in reservoir quality rocks and other locations deemed by mutual agreement of DOE and Rice to be appropriate. The initial ocean locations are Blake Ridge, Hydrate Ridge, Peru Margin and GOM. The permafrost location is Mallik. Although the ultimate goal of the project is to understand processes that control production potential of hydrates in marine settings, Mallik will be included because of the extensive data collected in a producible hydrate accumulation. To date, such a location has not been studied in the oceanic environment. The project will work closely with ongoing projects (e.g. GOM JIP and offshore India) that are actively investigating potentially economic hydrate accumulations in marine settings.

The overall approach is fivefold: (1) collect key data concerning hydrocarbon fluxes which is currently missing at all locations to be included in the study, (2) use this and existing data to build numerical models that can explain gas hydrate variance at all four locations, (3) simulate how natural gas could be produced from each location with different production strategies, (4) collect new sediment property data at these locations that are required for constraining fluxes, production simulations and assessing sediment stability, and (5) develop a method for remotely quantifying heterogeneities in gas hydrate and free gas distributions. While we generally restrict our efforts to the locations where key parameters can be measured or constrained, our ultimate aim is to make our efforts universally applicable to any hydrate accumulation.

Task 5: Carbon Inputs and Outputs to Gas Hydrate Systems
Jerry Dickens and Glen Snyder

As a result of discussions with Carolyn Ruppell at the January DOE gas hydrates workshop in Atlanta, Glen Snyder is presently assisting Andrew Hunt of the USGS Noble Gas laboratory in Colorado to develop sampling methods for determining noble gas isotopic composition of interstitial pore fluids and gas hydrate recovered from piston coring. Snyder will test the apparatus that they develop on a research cruise this June to recover gas hydrates from the Sea of Japan. The cruise is led by Ryo Matsumoto of the University of Tokyo and sponsored by the Japanese Ministry of Economy, Trade, and Industry. After the cruise, the apparatus and techniques will then be applied to gas hydrate research in the Gulf of Mexico with the USGS team.

The basic idea behind the study is that diagenesis of organic matter releases xenon gas along with hydrocarbons and the xenon is subsequently trapped in hydrate. Other noble gases such as helium diffuse directly through the hydrate. By measuring the noble gas isotopic composition, we hope to see if the hydrate is derived from thermogenic or biogenic sources (Figure 1). We also hope to determine whether the hydrate itself is presently growing or dissociating, or if it is in steady state.

Subtask 6.8: Sulfate profile as indicator of methane flux.

At the DOE workshop in Atlanta in January, Glen Snyder presented the work of Snyder and Dickens on modeling reaction rates above gas hydrate systems at the sulfate-methane transition. In addition to discussing mass balance of carbon and sulfur, the presentation demonstrated the observed stable carbon isotopic compositions are due to the admixture of deeply-sourced dissolved inorganic carbon and bicarbonate derived from anaerobic methane oxidation.

Other:
On March 29, G. Snyder, G. Dickens, and B. Dugan met with engineers from FUGRO Geotechnical Services on the Rice campus. The purpose of the meeting was to discuss both the needs and research requirements of industry around gas hydrates, as well as the research interests of academia. Since the FUGRO offices and Rice are only a short drive from each other, we plan to meet with them in the future, as well as visit their research vessels then they arrive in Galveston.

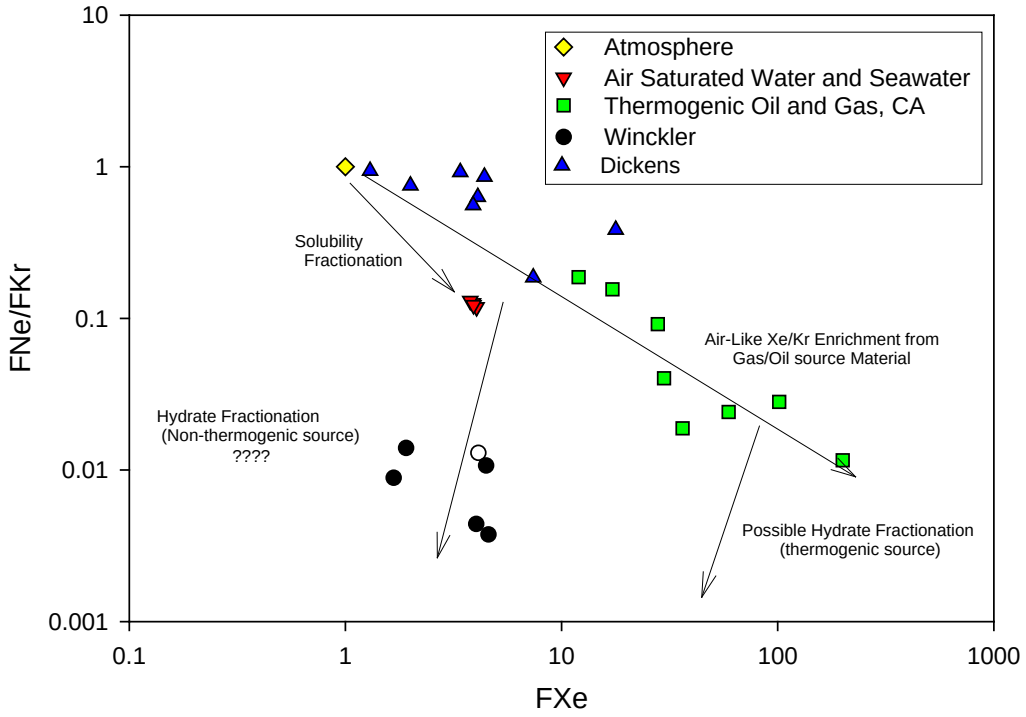

Figure 1. Plot of FNe/FKr vs FXe. $Fi = i/^{36}Ar_{sample} / i/^{36}Ar_{atmosphere}$

Presented in Figure 1 is a summary of the noble gas data compiled from Dickens and Kennedy (2000) and Winckler et al. (2002)coupled with atmospheric and solubility values. Included in the figure is noble gas data taken from Torgersen and Kennedy (1999) which shows the Kr and Xe enrichment associated with thermogenic methane samples from the Elk Hills oil and gas fields of California. Torgersen and Kennedy (1999) discovered that Kr and Xe concentrations in the thermogenic natural gas samples are highly enriched relative to atmosphere, but still retain air-like isotopic composition. The cause of the enrichment was greater than could be explained by simple fluid-water-oil mass partitioning of the noble gases and had to be derived by elevated concentrations of Kr and Xe in the original organic matter that comprised the source material for the natural gas. Knowing that thermogenically derived methane is enriched in heavy noble gas isotopes we expect the hydrates derived from this gas would be even more enriched in the heavy nobles and would plot at much higher FXe than biogenically derived gases. In both cases hydrate related gas will have a distinctive fractionation pattern that can be used to distinguish hydrate related gas from non-hydrate related biogenic and thermogenic reservoirs.

References

Chaduteau, C., Fourré, E., Jean-Baptiste, P., Dapoigny, A., Baumier, D., and Charlou, J., 2007, A new method for quantitative analysis of helium isotopes in sediment pore-waters Limnology and Oceanographic: Methods, v. 5, p. 425-432.

Dickens, G. R., and Kennedy, B. M., 2000, Noble gases in methane hydrate from the Blake Ridge, *in* Miller, C. M., and Reigel, R., eds., Proceedings of the Ocean Drilling Program; volume 164; scientific results; gas hydrate sampling on the Blake Ridge and Carolina Rise; covering Leg 164 of the cruises of the drilling vessel JOIDES Resolution, Halifax, Nova Scotia, to Miami, Florida, sites 991-997, 31 October-19 December 1995, Texas A & M University, Ocean Drilling Program, College Station, TX, United States (USA).

Torgersen, T., and Kennedy, B. M., 1999, Air-Xe enrichments in Elk Hills oil field gases; role of water in migration and storage: Earth and Planetary Science Letters, v. 167, no. 3-4, p. 239-253.

Winckler, G., Aeschbach-Hertig, W., Holocher, J., Kipfer, R., Levin, I., Poss, C., Rehder, G., Suess, E., and Schlosser, P., 2002, Noble gas and radiocarbon in natural gas hydrates: Geophysical Research Letters, v. 29, no. 10, p. 4.

Task 6: Numerical Models for Quantification of Hydrate and Free Gas Accumulations

Subtask 6.3. Compositional Effect on BSR, Synthetic Seismic Response

Guangsheng Gu

In this subtask, we have established the ability to generate synthetic seismogram with Ricker wavelets on some cases of hydrate/gas transition.

From the work we have finished, we can find out existence of another gas component in marine hydrate system, can affect the hydrate and gas distribution greatly. As an example, in a CH_4-C_3H_8-H_2O hydrate system, there can exist a transition region in which Aq, H (sII) and V can co-exist, and S_H and S_v can change gradually (Fig. 6.3.1.). The transition zone can be as thick as 300 m. The p-wave velocity Vp, can vary gradually throughout this transition zone (Fig. 6.3.2).

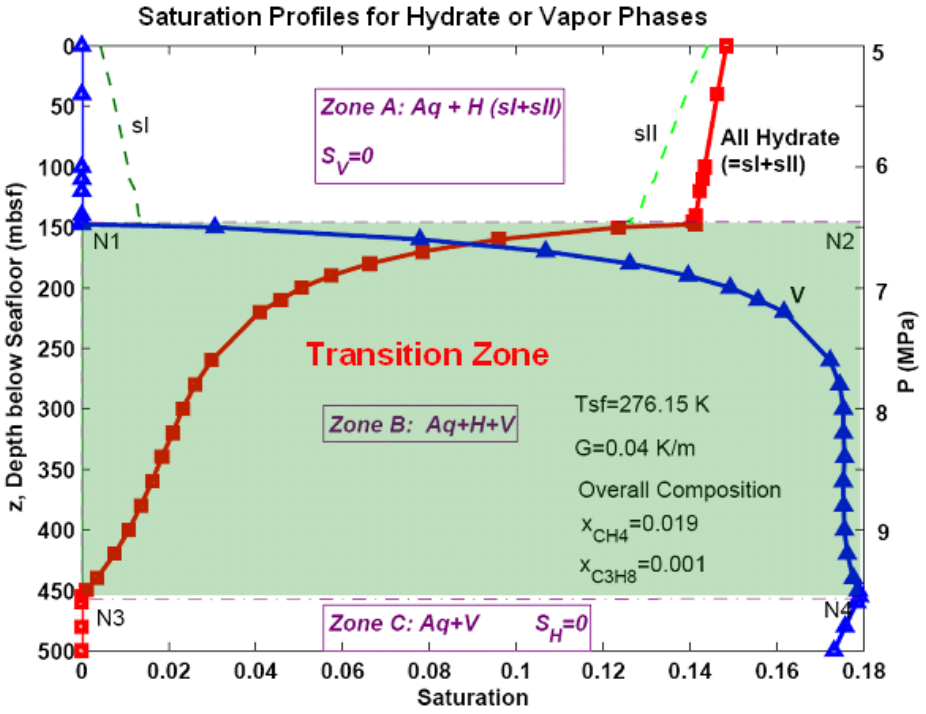

Figure 6.3.1. An example calculation of a CH_4-C_3H_8-H_2O System (water-free propane molar fraction is 0.05; Overall composition x_{CH4}=0.019, x_{C3H8}=0.001, x_{H2O}=0.98).

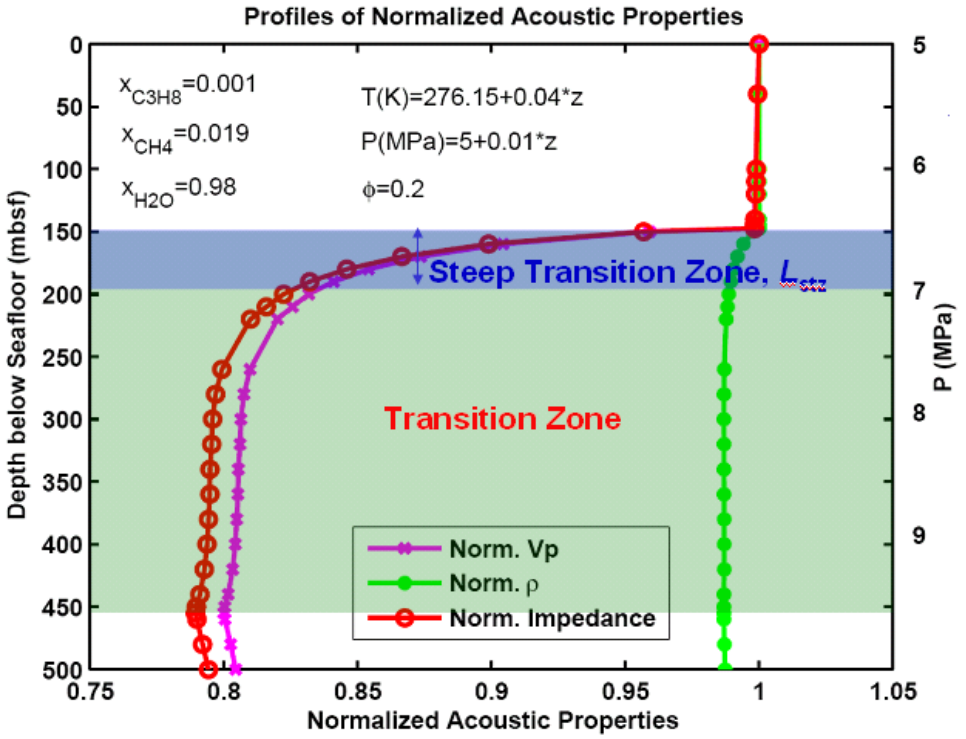

Figure 6.3.2. An example calculation of a CH_4-C_3H_8-H_2O System (Profiles of Normalized Acoustic Properties of the CH_4-C_3H_8-H_2O Hydrate System. Impedance $Z = \rho V_p$. Data are normalized so that at seafloor the value is 1).

By simplification, we can have two different types of Vp profiles from seafloor to deeper sediment shown in Fig. 6.3.3 – 6.3.4. There impulse responses are also shown in these figures. We can see that the seismic response, at Base of GHSZ (BGHSZ) for pure methane hydrate system (abrupt Vp change), the amplitude of reflection at BGHSZ is in the similar order of magnitude of that at seafloor (Fig. 6.3.3.).

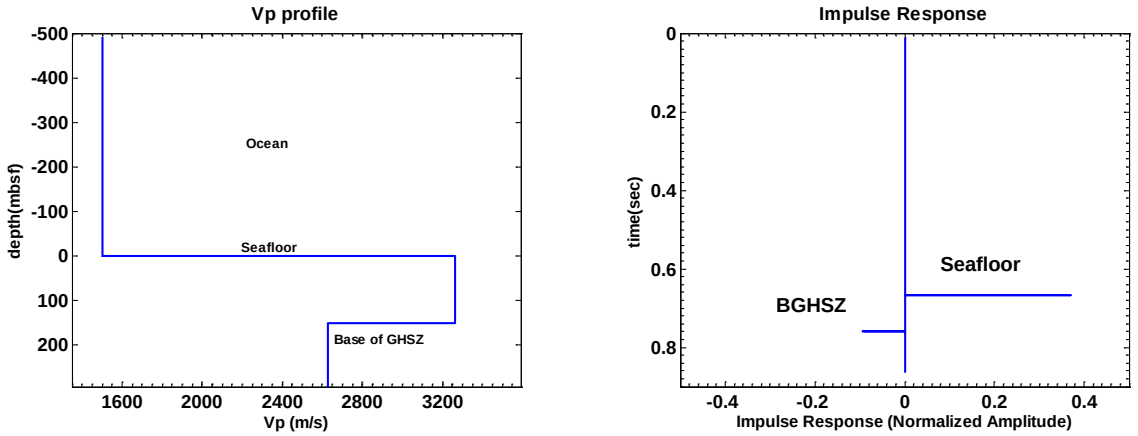

(a) V_p Profile (b) Impedance Response

Figure 6.3.3. Abrupt Vp Change System: V_p Profile and Impedance Response

However, in a mixed hydrate system, the Vp profile varies gradually at hydrate/gas transition zone, their impulse response at this gradual transition zone, is much weaker than that at seafloor (Fig. 6.3.4.), though not zero.

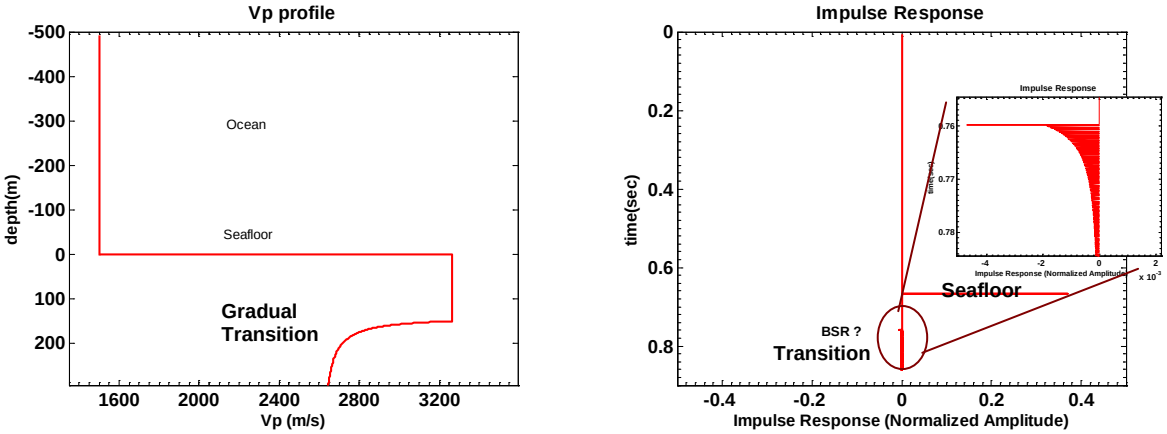

(a) V_p Profile (b) Impedance Response

Figure 6.3.4. Mixed-hydrate System (Graduate V_p Change): V_p Profile and Impedance Response

Some certain Ricker wavelets are used to 1D synthetic seismic profile. A Ricker wavelet has a smooth power spectrum curve, with a peak frequency (Fig. 6.3.5). They are widely used in seismic simulators. In exploration seismic simulation, the peak frequency is mostly within a range from 10 to 100 Hz, and 30 Hz is a typical frequency.

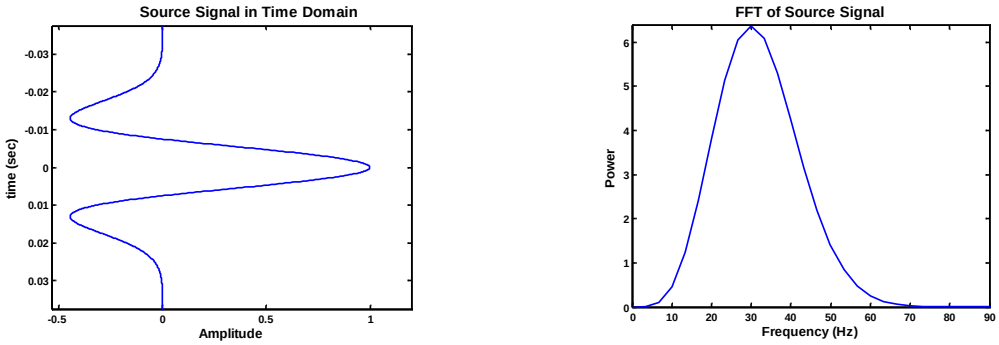

(a) Source Signal in Time Domain (b) Power Spectrum of Source Signal

Figure 6.3.5. Example of Source Signal: Ricker Wavelet (Here Peak Frequency: 30 Hz)

By using Ricker wavelets, with frequency from 10 to 100 Hz, we obtained the synthetic seismogram (Fig. 6.3.6.), both for that from a step change Vp profile (i.e., for pure methane hydrate system), and for that from a gradual transition zone. For the same thickness of the steep transition zone (shown in Fig. 6.3.2.) L_{stz}, different peak frequencies are used; for each wavelet with a certain peak

frequency, the characteristic wavelength is denoted as λ. The thickness ratio L_{stz}/λ are calculated. The seismograms are shown in Fig. 6.3.6.

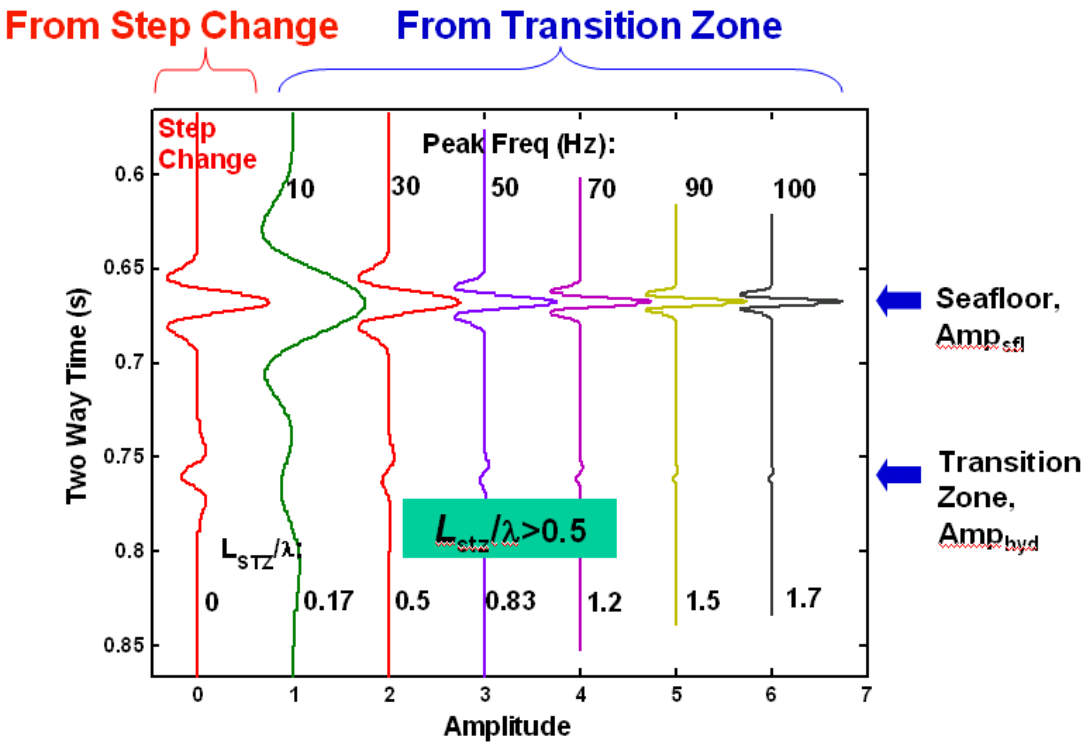

Figure 6.3.6. Reflection as a Function of L_{stz}/λ.

To quantitatively understand the seismic response, the amplitude ratio, Ratio of Amplitude at Hydrate/Gas Transition, to that at Seafloor, A_{Hdr}/A_{sfl}, is defined. If $A_{Hdr}/A_{sfl} \leq 0.1$, the reflection will be called a "weak reflection" (i.e., weak BSR). The relationship between A_{Hdr}/A_{sfl} and thickness ratio L_{stz}/λ is plotted in Fig. 6.3.7. We can find out both qualitatively (in Fig. 6.3.6.) and quantitatively (in Fig. 6.3.7.) that:

If $L_{stz}/\lambda > 0.5$, then $A_{Hdr}/A_{sfl} \leq 0.1$, i.e., a weak reflection will be observed.

In Fig. 6.3.7., $A_{Hdr}/A_{sfl} \leq 0.1$ refers to that peak frequency is higher than 30 Hz (roughly). But 30 Hz is a typical frequency. Therefore, if a xed-hydrate transition zone exists, it's possible to observe a "weak BSR".

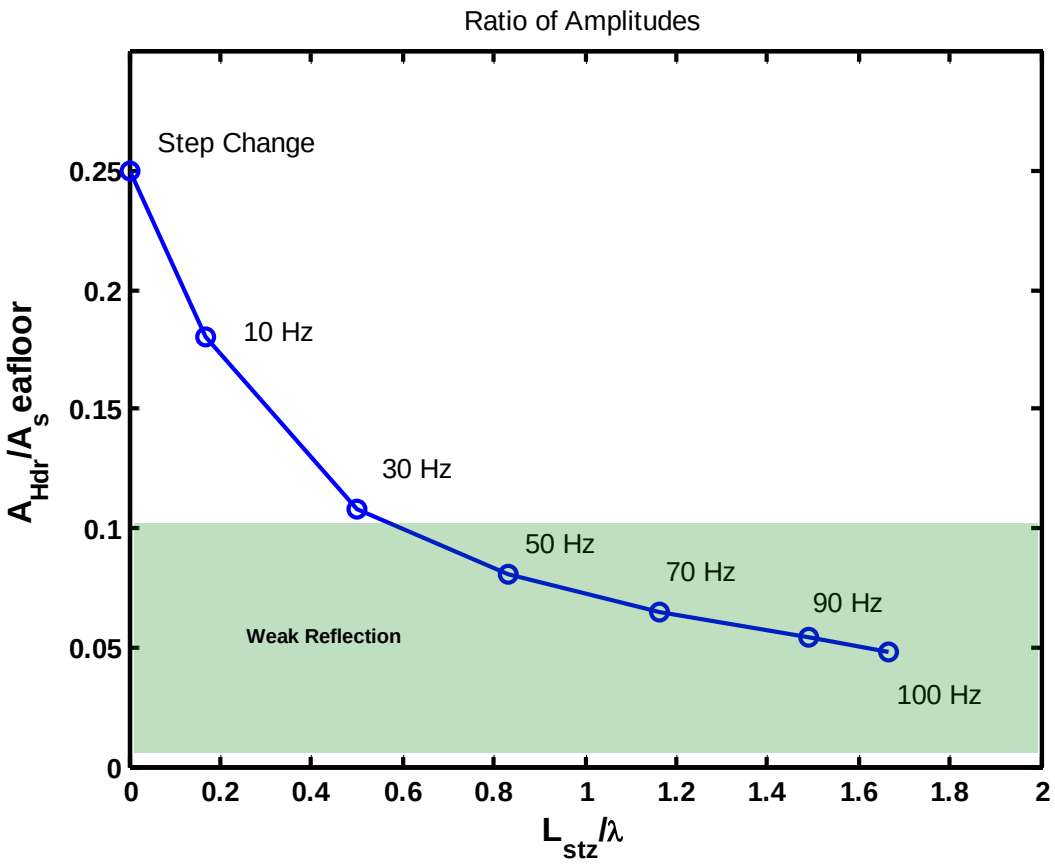

Figure 6.3.7. Amplitude Ratio as a Function of L_{stz}/λ.
(The Ratio of Amplitude at Hydrate/Gas Transition, to that at Seafloor, A_{Hdr}/A_{sfl}).
If $A_{Hdr}/A_{sfl} \leq 0.1$, the reflection is called a "weak reflection", as shown in the shadowed region. The peak frequency for each point is also labeled.

Subtask 6.4. Blanking and chaotic zones due to hydrate distribution.
Guangsheng Gu

We have started working on acoustic velocity profiles in different types of sediment layers. Due to hydrate accumulation, the velocity in different types of sediment layers can become similar with each other.

Geological settings:

We set several horizontal layers with different properties, from seafloor to deeper sediment. These layers are in 2 types: sandstone or clay/shale. Sandstone layers have higher porosity (20%~30%), and shale layers with some porosity values varying with depth (Fig. 6.4.1). Assume hydrate saturation increases gradually. Then we estimated the Vp density, and seismic impedance profiles of these two different types of layers, and made comparison between them.

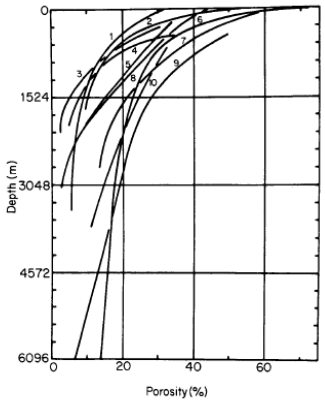

Fig 2.2 Porosity of clay/shale as a function of depth [Jenyon 1990 (Magara 1980)]

Figure 6.4.1. Porosity of Clay/shale as a function of depth

Parameters:

Table 6.4.1: Acoustic properties of components

Component	***V*p (m/s)**	**ρ (kg/m3)**
Sea Water (w)	1500	1030
Hydrate (H)	3300	900
Mineral1 (m1, sandstone)	2000~4000	2500

Mineral2 (m2, shale)	2400	2600

Table 6.4.2: other parameters

Parameter	**Value**	
Porosity1 (in sandstone layer)	0.2 ~ 0.3	
Porosity2 (in shale layer)	Up: 0.6; Low: 0.2~0.4	
Sh	0~1	

Equations:

Estimate average density and Vp according to these equations:

$$\overline{\rho} = (1-\phi)\rho_m + \phi\sum_i S_i\rho_i$$

$$\frac{1}{V_p} = \frac{\phi(1-S_H-S_V)}{V_w} + \frac{\phi S_H}{V_H} + \frac{(1-\phi)}{V_m} + \frac{\phi S_V}{V_V}$$

V_p --- average compressional velocity of the sediment;

V_H --- compressional velocity of the pure hydrate;

V_w --- compressional velocity of the fluid;

V_m --- compressional velocity of the mineral;

ϕ --- porosity (as a fraction);

S_H --- Hydrate saturation

S_V --- Vapor (Gas) saturation

Impedance: $Z = \rho V_p$

Preliminary result:

The preliminary results show that the acoustic impedance of sandstone layer, is possible to be lower than that of a shale layer; then when hydrate saturation

increases, it's possible to increase to higher values than that of a shale layer. In these situations, it's possible that a blanking can be achieved during the hydrate accumulation process. (Figures.)

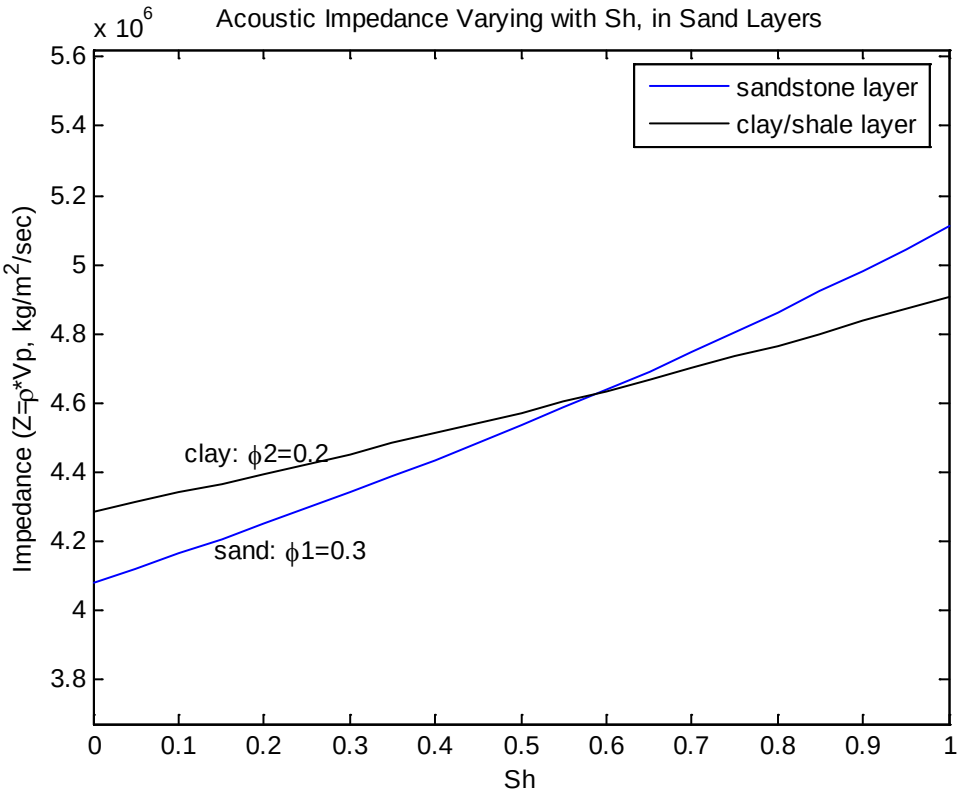

Figure 6.4.1: Impedance increase of sandstone layer due to S_h increase

Parameters: ϕ_1=0.3; ϕ_2=0.2; V_{p_sand}=2300 m/s; V_{p_clay}=2000 m/s

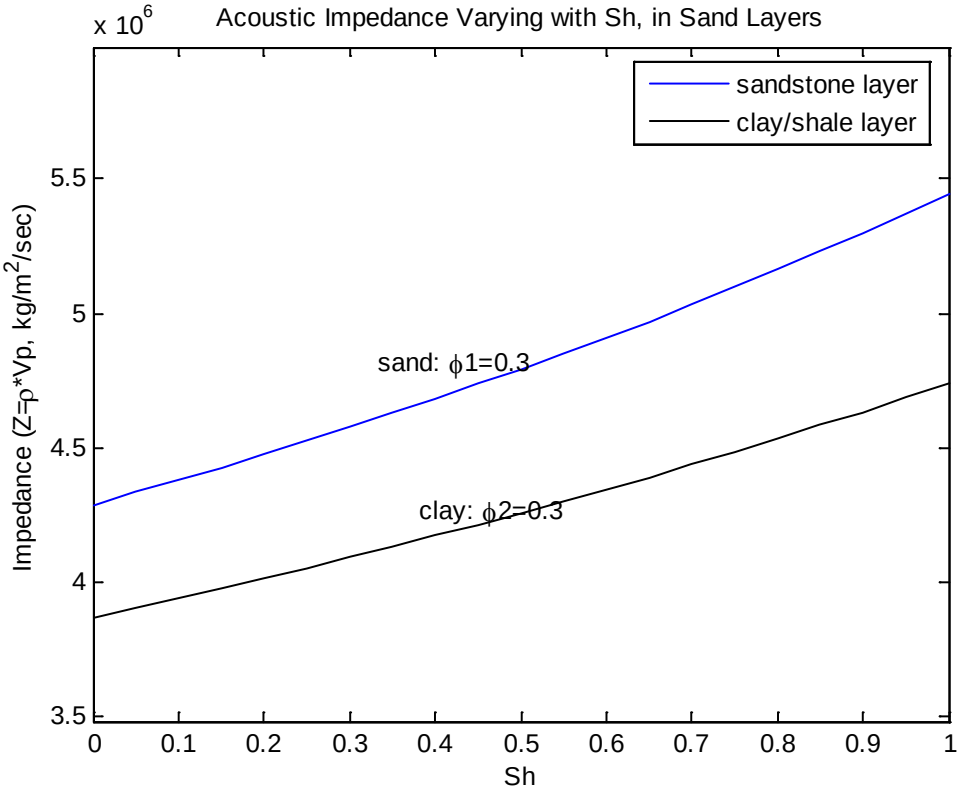

Figure 6.4.2: Impedance increase of sandstone layer due to S_h increase

Parameters: ϕ_1=0.3; ϕ_2=0.3; V_{p_sand}=2500 m/s; V_{p_clay}=2000 m/s

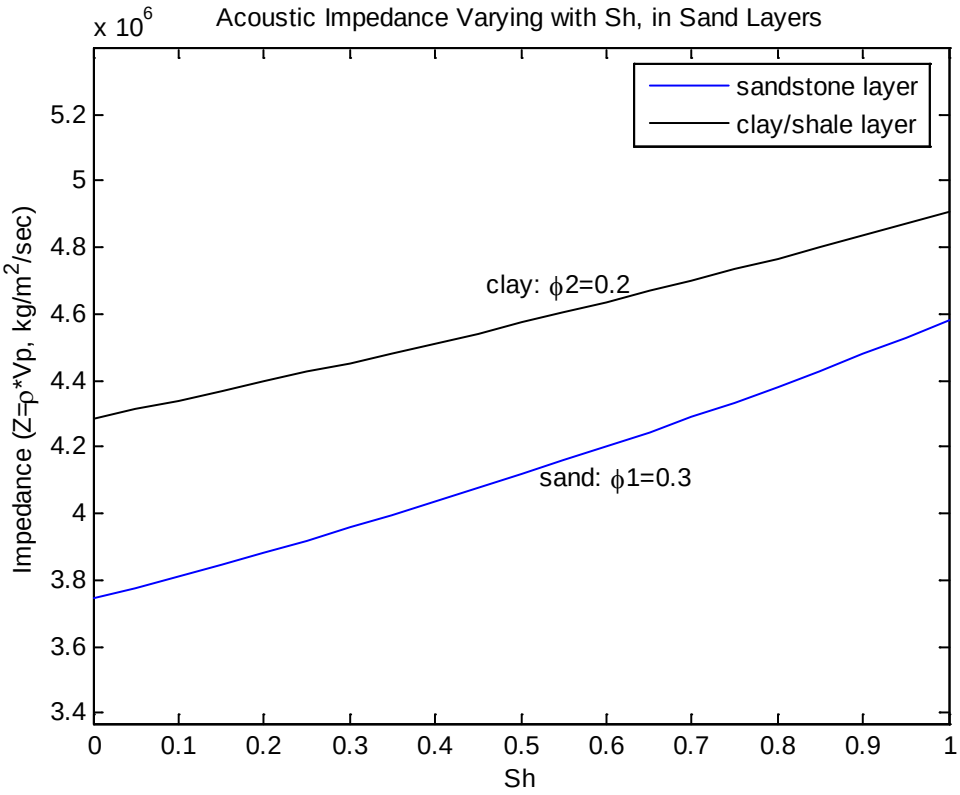

Figure 6.4.3: Impedance increase of sandstone layer due to S_h increase

Parameters: ϕ_1=0.3; ϕ_2=0.3; V_{p_sand}=2000 m/s; V_{p_clay}=2000 m/s

Subtask 6.8 (b): Sulfate, bicarbonate, calcium and carbon isotope ($\delta^{13}C$) profiles as an indicator of methane flux above marine gas hydrate systems**:** *Sayantan Chatterjee*

Abstract

Methane flux is an important constraint on the amount of hydrate that may be present in marine sediments. One approach to determine this flux is to use the depth to the sulfate-methane transition (SMT). Pore-water sulfate concentrations deplete to zero in shallow sediments above methane hydrate systems. Many authors attributed these chemical gradients to anaerobic oxidation of methane (AOM) at the SMT and directly related the depth of the SMT to the upward methane flux at steady-state conditions. However, an alternative mechanism for sulfate consumption by particulate organic carbon (POC) has been interpreted by various authors. To reconcile these two interpretations, *Bhatnagar and others'* 1D model (2008) was extended and methane, sulfate, dissolved inorganic carbon (DIC), calcium and carbon isotope concentration profiles were computed with both advective and diffusive fluxes. In addition to the mass balances, sulfate consumption reactions following two reaction pathways (i.e.: POC driven and AOM) have been included in the model. In most marine gas hydrate systems, it is shown that cross-plot of fluxes of sulfate and DIC around the SMT lie on a 1:1 line and justifies the dominance of AOM for sulfate consumption in shallow sediment. For insignificant fluxes, relative to sulfate reduction by POC, the concentration cross-plot lie on the 2:1 line justifying the alternative reaction mechanism by POC. The numerical model developed in this report serves as a tool to interpret upward methane fluxes with the help of pore water profiles.

Introduction

The amount of gas hydrate is controlled by dynamic inputs and outputs of methane over geologic timescales (Dickens, 2003; Buffett and Archer, 2004). The upward methane flux is an important constraint on the amount and distribution of hydrates. In the shallow sediments (~30 mbsf) above all gas hydrate systems there exists a sulfate-methane transition (SMT) zone where pore water sulfate gets depleted to near-zero concentration, generally underlain by rapid increase in methane concentrations.

For most gas hydrate systems, one potential approach for determining methane flux is to use the depth to the SMT (L_s, Figure 6.8.1). Many authors have attributed depletion in pore water sulfate at the SMT to anaerobic oxidation of methane (AOM). Indeed, if AOM dominates consumption of methane and sulfate and the system is at steady-state conditions, the depth of the SMT should be directly related to the upward flux of methane (Borowski *et al.*, 1996; Snyder *et al.*, 2007; Dickens and Snyder, 2007).

The sulfate sink in these systems involves dissolved methane to consume sulfate at the SMT as shown in (1).

(1) $$CH_4\ (aq) + SO_4^{2-} \rightarrow HCO_3^- + HS^- + H_2O$$ AOM

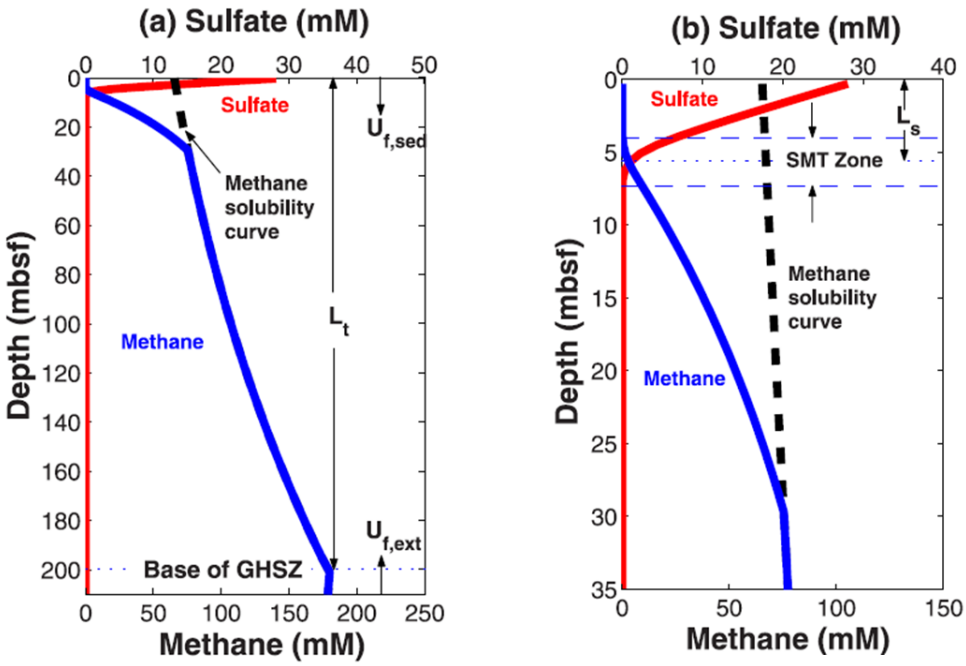

Figure 6.8.1: (a) Schematic representation of a gas hydrate system showing pore water sulfate and methane concentrations, which go to zero at shallow depths due to AOM. The dashed line represents the methane solubility curve. Fluid fluxes due to compaction driven flow and external flow are denoted as $\boldsymbol{U_{f,sed}}$ and $\boldsymbol{U_{f,ext}}$, respectively; $\boldsymbol{L_t}$ is the depth to the base of the gas hydrate stability zone. **(b)** Zoomed sulfate-methane transition (SMT) zone showing an overlap of sulfate and methane profiles and its depth below the seafloor ($\boldsymbol{L_s}$) (Bhatnagar *et al*., 2008).

Previous numerical modeling attempts have also shown that the net upward flux controls the pore water methane and sulfate concentration profiles and is thus related to the SMT depth (Bhatnagar *et al*., 2008). Furthermore, the thickness of the hydrate zone and the gas hydrate saturation have been reported to be direct functions of the upward methane flux (Davie and Buffett, 2001; Bhatnagar *et al*., 2008). Several studies have shown correlation between the SMT depth and the shallowest occurrence of gas hydrate (Borowski *et al.*, 1999). Few specific sites suggested a “rule of ten” where the shallowest gas hydrate occurs at a depth 10 times of the SMT (Paull *et al*., 2005). Using a generalized one-dimensional (1D) numerical model, validated by an analytical theory (*Bhatnagar et al.,* 2010), Bhatnagar and coworkers estimated that the top of the gas hydrate layer occurs at 10-12 times of the SMT depth (Bhatnagar *et al*., 2008). Thus, one-to-one relationships exist between the SMT depth; and the

upward methane flux, the gas hydrate layer thickness and the gas hydrate saturation within the GHSZ.

In addition to AOM, particulate organic carbon (POC) can also consume pore water sulfate in shallow sediments. In the absence of methane, bacteria use the POC as a substrate to consume sulfate (Berner, 1980; Boudreau and Westrich, 1984). This reaction involves the oxidation of organic carbon and the reduction of sulfate to produce DIC and hydrogen sulfide shown in (2):

(2) $$2CH_2O\,(s) + SO_4^{2-} \rightarrow 2HCO_3^- + H_2S$$ POC

Notably, the amounts of reactants and products in the two reactions are different. In (1) HCO_3^- :SO_4^{2-} stoichiometry is 1:1, whereas in (2) it is 2:1.

Presently, the use of sulfate profiles and the SMT depth to calculate upward methane fluxes is controversial because various authors have interpreted pore water composition and carbon isotope data in shallow sediment differently, even at the same sites (Kastner et al., 2008; Dickens and Snyder, 2009). The roots of the problem are twofold: (1) sulfate consumption can occur through two reaction pathways, and (2) dissolved inorganic carbon (DIC), a reaction constituent, has multiple sources and sinks.

Bhatnagar and co-workers developed a generalized 1D numerical model for gas hydrate accumulation in marine sediments over geologic timescales (Bhatnagar *et al.,* 2007). Previous 1D model computed methane and sulfate profiles, however, DIC, calcium and carbon isotopes were not coupled with methane and sulfate mass balance equations. In this report, both the interpretations regarding the sulfate reduction stoichiometry and the carbon isotope balance are revisited and Bhatnagar's 1D model (Bhatnagar *et al*., 2007, 2008) was extended. Hence, both the sulfate consumption reactions (POC and AOM) were included and mass balances of all the carbon and sulfate species in the system were coupled.

Example site – Hydrate Ridge, 1244, Cascadia margin

As an example, physical properties and seafloor conditions were chosen similar to Hydrate Ridge site 1244 from the Ocean Drilling Program (ODP) leg 204 data to simulate the pore water chemistry profiles. This site is located at 890m below sea level (mbsl) on the eastern flank of the Hydrate Ridge about 3km northeast of the southern summit (Trehú *et al.*, 2003). The seafloor temperature (276.8 K) and pressure are well within the range for hydrate stability and occurrence and the linear geothermal gradient is 0.061°C/m. For these parameters, our calculations show that the temperature profile intersects the three-phase equilibrium curve at about 133.4 m below seafloor and marks the base of the GHSZ. Sedimentation rate is 27 cm kyr^{-1} and porosity of the sediments at the seafloor, is about 70% (Trehú *et al.*, 2003). Other parameters that are specific to site 1244, used in this model are listed in appendix. The

concentration profiles of sulfate, methane, alkalinity (DIC), and calcium in pore water and carbon isotope $\delta^{13}C$ data in DIC obtained from leg 204 data for hole 1244 are shown in Figure 6.8.2 (Trehú *et al.*, 2003). Note methane (red) and sulfate (blue) concentrations are shown in the same plot. Methane concentrations are low because significant quantity of methane was lost during its measurement. Notably, in 1244, the SMT is located at ~8.5 mbsf, where pore water sulfate approaches zero concentration and the remaining interstitial water species show a distinguishable change in slope at the same depth.

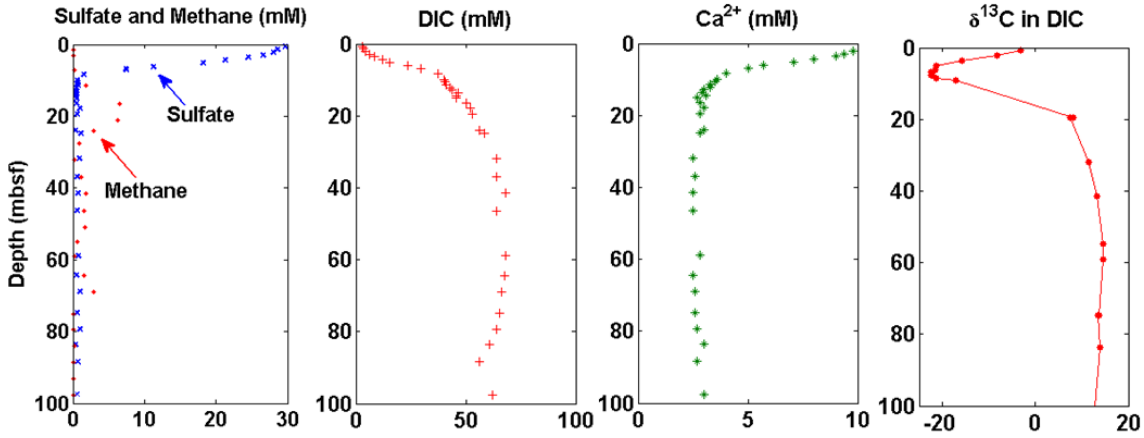

Figure 6.8.2: Sulfate, methane, alkalinity (DIC), calcium concentration profiles and carbon isotope $\delta^{13}C$ composition in DIC for shallow sediment at site 1244 on Hydrate Ridge (original data from Trehú *et al.*, 2003)

Two contradictory hypotheses

The two contradictory hypotheses revolve around the dominance of two reactions for sulfate consumption namely; AOM and POC driven consumption as stated earlier. Borowski *et al*. (1996) initially interpreted how sulfate gradients may be used as a proxy to measure in-situ methane fluxes from underlying hydrate sediments at sites where linear sulfate profiles exist. Linear sulfate profiles in shallow sediments indicate that sulfate profile is primarily driven by diffusion to the SMT where it reacts at the SMT with the methane flux from below. This is in contrast to reaction with POC which is distributed throughout the sediment. If AOM is the dominant reaction, then at steady state conditions, sulfate and methane fluxes should be balanced (Borowski *et al.*, 1996), and the pore water sulfate concentration profile is determined by the upward methane flux originating from deeper sediments.

<u>Argument for POC reaction</u>

Several investigators (Kastner *et al.*, 2008) have attempted to discriminate between the two reactions using pore water concentration profiles and carbon isotope data. In particular, arguments for the dominance of POC reaction over AOM have been made using cross-plots of change in excess alkalinity versus change in sulfate concentration (Figure 6.8.3). Excess alkalinity is the amount of HCO_3^- (more commonly DIC) that would occur in pore water if authigenic carbonate had not precipitated. The change in excess alkalinity can be computed by summing the deviations in pore water alkalinity, Ca^{2+} and Mg^{2+} relative to their respective concentration in seawater. The change in pore water sulfate concentration is relative to the seawater. In the case shown here (Figure 6.8.3), there is a 2:1 slope, which Kastner and others interpret as release of two moles of DIC due to consumption of one mole of sulfate. If this interpretation is correct, this would imply POC driven sulfate consumption in a closed system (Kastner *et al*., 2008). A closed system is one in which sulfur and carbon fluxes in and out of sediment horizons are zero. This situation does not occur in most areas with gas hydrate because fluxes through diffusion and advection are usually faster than through sedimentation.

The carbon isotope composition ($\delta^{13}C$) of DIC across the SMT has also been used to infer the POC driven reaction mechanism (Kastner *et al*., 2008). The overall idea is that POC has a $\delta^{13}C$ of -25‰ whereas biogenic methane has a $\delta^{13}C$ of -60‰, so the isotope composition of DIC at the SMT should give the proportion generated from AOM and POC. For example, the nominally -25‰ of DIC across the SMT at site 1244 has been argued to reflect a dominance of POC consumption of sulfate.

Argument for AOM reaction

An analysis of reactants and products using fluxes is a much better approach for understanding the stoichiometry of the sulfate consumption reaction. This is particularly true because there is often a flux of DIC into the SMT from below (Dickens and Snyder, 2009). Specifically, at ODP site 1244, when one calculates fluxes of DIC, there are −6 mol/m^2kyr of HCO_3^- entering the SMT from below and −22 mol/m^2kyr of HCO_3^- are leaving the SMT towards the seafloor. This gives a net change of −16 mol/m^2kyr of HCO_3^- across the SMT. This net change of HCO_3^- flux nicely balances the +16mol/m^2kyr of $S0_4^{2-}$entering the SMT, suggesting a 1:1 stoichiometry (Dickens and Snyder, 2009).

The source of deep flux of DIC is from the biogenic generation of methane occurring in deeper sediments. The methanogenesis reaction involves breakdown of two moles of POC to form one mole of methane and one mole of carbon dioxide under microbial action via a series of reactions as shown below.

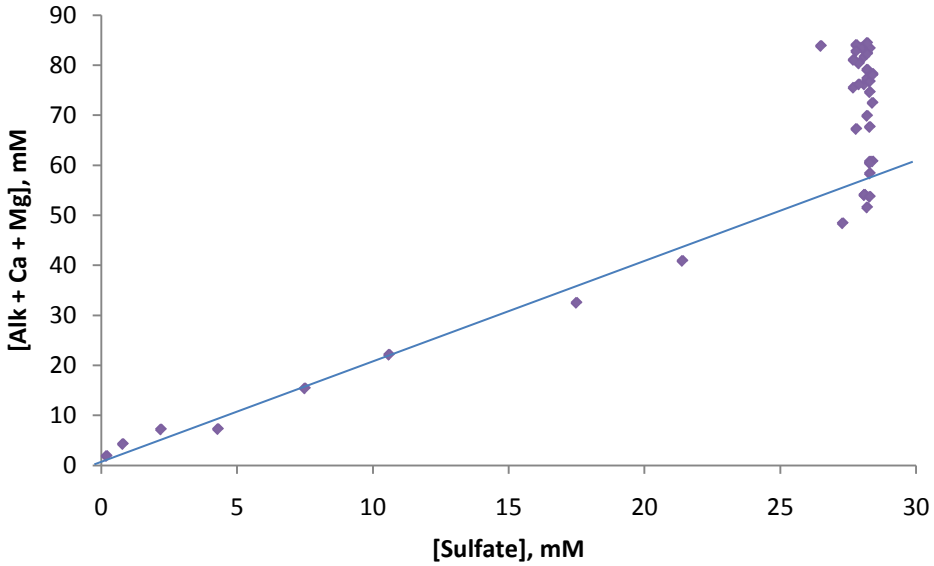

Figure 6.8.3: Concentration cross-plot of "excess alkalinity" corrected for carbonate precipitation versus SO_4^{2-}(mM) relative to the seafloor for shallow sediment at site 1244 on Hydrate Ridge (original data from Trehú *et al.*, 2003). As emphasized by Kastner *et al.* (2008), there is a 2:1 relationship for pore water concentrations above the SMT. Note, however, that excess alkalinity continues to rise below the SMT. There is an upward flux of HCO_3^- from deeper sediment, which necessarily implies that only a fraction of excess alkalinity above the SMT comes from shallow sediment

Methanogenesis reaction is a biochemical reaction and can be represented as a series of the following reactions.

Fermentation: $6CH_2O + 2H_2O \rightarrow 2CH_3COOH + 2CO_2 + 4H_2$

CO_2 reduction and acetate methanogenesis

$$CO_2 + 4H_2 \rightarrow CH_4 + 2H_2O$$
$$2CH_3COOH \rightarrow 2CH_4 + 2CO_2$$

Overall reaction: $2CH_2O \rightarrow CH_4 + CO_2$

The carbon dioxide reacts with pore water to form DIC: $CO_2 + H_2O \rightarrow HCO_3^- + H^+$

The overall methanogenesis reaction is shown below in (3).

(3) $2CH_2O\,(s) + H_2O \rightarrow CH_4 + HCO_3^- + H^+$

Over geologic timescales, sedimentation and deposition of older sediments buries the organic carbon to greater depths. This gives rise to the deeper DIC flux coming from below. However, DIC formed during methanogenesis typically has an isotope composition of +10‰ or greater. This means that, in an open system, the measured $\delta^{13}C$ of DIC across the SMT is the

net result of $\delta^{13}C$ formed by reactions at the SMT (e.g., AOM) and DIC fluxing in to and out of the SMT. A DIC of -25‰ across the SMT can result from AOM and a deep DIC flux with a $\delta^{13}C$ of +10‰ or greater (Dickens and Snyder, 2009). So, an observed value of $\delta^{13}C$ of DIC of -25‰ at the SMT need not be concluded to be a result of POC driven sulfate consumption. It could also be due to combined effect of AOM and deep source of DIC as a result of methanogenesis. To reconcile these two hypotheses, a mathematical model has been formulated and presented in the following section.

Numerical model

Gas hydrate accumulation in marine sediment has been modeled for 1D systems by Bhatnagar and others (Bhatnagar *et al*., 2007). Their overall modeling framework incorporated phase equilibrium and methane solubility calculations in addition to sediment deposition, porosity reduction and mass conservation for methane, water, and organic content. The model included advective and diffusive fluid fluxes as a result of compaction, and upward fluid flow arising from deeper sediments. However, the model did not couple bicarbonate, calcium, and carbon isotope composition along with methane and sulfate mass balances. All gas hydrate systems harbor few primary chemical reactions involving various pore water chemical species as listed below. The following three reactions are expressed with their corresponding kinetic models defining the kinetic rate for the respective reactions; and the fourth reaction is a reversible reaction and the equilibrium model is shown as follows:

(i) Methanogenesis and fermentation reaction in deeper sediments

$$2CH_2O + H_2O \rightarrow CH_4 + HCO_3^- + H^+ \qquad r_{meth} = -\lambda\alpha$$

(ii) AOM reaction at the SMT

$$CH_4 + SO_4^{2-} \rightarrow HCO_3^- + HS^- + H_2O \qquad r_{AOM} = -\lambda_{AOM} c_m^l c_s^l$$

(iii) POC driven sulfate consumption between the seafloor and the SMT

$$2CH_2O + SO_4^{2-} \rightarrow 2HCO_3^- + H_2S \qquad r_{POC} = -\lambda_{POC}\alpha c_s^l$$

(iv) Calcite precipitation reaction

$$HCO_3^- + Ca^{2+} \rightarrow H^+ + CaCO_3\downarrow \qquad r_{ppt} = \frac{\Delta c^l_{CaCO_3}}{\Delta t}$$

The methanogenesis rate of reaction is represented by λ; whereas the rates of reaction for sulfate reduction by POC and AOM are denoted by λ_{POC}, and λ_{AOM}, respectively. Unlike the kinetic modeling for the irreversible reactions, equilibrium rate for the calcite precipitation reaction is modeled differently as a function of formation of calcium carbonate. The authigenic carbonate precipitation is an

equilibrium reaction and its rate is quantified by the amount of calcium carbonate formed in unit time. The phase concentration for the different species are represented as c_m^l for methane, c_s^l for sulfate, c_b^l for DIC, c_{ca}^l for calcium, $c_{CaCO_3}^l$ for calcium carbonate and α for POC. Hydrogen ions that are being formed in the system as a product of different reactions are assumed to be transported by advection and diffusion, thereby avoiding accumulation of hydrogen ions which would eventually make the formation acidic and the reactions would eventually stop. However, the hydrogen ion transport is not modeled in this work.

Organic Material Balance for in-situ production

The organic carbon content available for methanogenesis (α) is represented as a mass fraction of the total sediment. However, α represents only a fraction of the total organic carbon (TOC) since the entire content is not converted to methane. The sedimentation rate ($\dot{S}$) and amount of degradable organic content at the seafloor is assumed to remain constant over time. Furthermore, the POC is modeled to advect downward with the sediment velocity v_s. With the above assumptions, the organic material balance is shown below.

$$\frac{\partial}{\partial t}[(1-\phi)\,\rho_{sed}\alpha] + \frac{\partial}{\partial z}[(1-\phi)\rho_{sed}\,v_s\alpha] = -\rho_{sed}\,\lambda(1-\phi)\alpha$$

Further, the material balance could be rewritten in terms of sediment and fluid fluxes instead of velocities. The material balance equation can be rewritten in a dimensionless form using the scaling scheme developed by Bhatnagar *et al*. (2007) and presented as follows.

$$\frac{\partial}{\partial \tilde{t}}\left(\tilde{\alpha}(1-\tilde{\phi})\right) + Pe_1\frac{\partial}{\partial \tilde{z}}\left[\left(\frac{1+\gamma}{\gamma}\right)\tilde{U}_s\,\tilde{\alpha}\right] = -Da(1-\tilde{\phi})\tilde{\alpha}$$

Methane Mass Balance

Following previous work (Bhatnagar *et al.*, 2007; 2008), the methane mass balance equations have been simplified to exclude the gas hydrate and free gas phase terms. Assuming methane generation from POC and consumption due to AOM reaction, the mass balance equations are illustrated below.

$$\frac{\partial}{\partial t}[\phi\,\rho_w\,c_m^l] + \frac{\partial}{\partial z}\left[U_f\,\rho_w\,c_m^l\right]$$

$$= \frac{\partial}{\partial z}\left[\phi\,\rho_w\,D_m\,\frac{\partial c_m^l}{\partial z}\right] + \frac{M_{CH_4}}{M_{POC}}\,\rho_{sed}\,\lambda(1-\phi)\alpha - \frac{\phi\;\lambda_{AOM}\,(\rho_w\,c_m^l)(\rho_w\,c_s^l)}{M_{SO_4}}$$

The terms on the left are the accumulation term followed by the convection term. The terms on the right hand side represent diffusion followed by the reaction terms. The reaction terms correspond to methanogenesis from POC and AOM, respectively. The mass balance equation can be rewritten in a dimensionless form using the same scaling scheme shown above.

$$\frac{\partial}{\partial \tilde{t}}\left[\left(\frac{1+\gamma\tilde{\phi}}{\gamma}\right)\tilde{c}_m^l\right] + \left(\frac{1+\gamma}{\gamma}\right)(Pe_1 + Pe_2)\frac{\partial \tilde{c}_m^l}{\partial \tilde{z}} = \frac{\partial}{\partial \tilde{z}}\left[\left(\frac{1+\gamma\tilde{\phi}}{\gamma}\right)\frac{\partial \tilde{c}_m^l}{\partial \tilde{z}}\right]$$
$$+ \frac{M_{CH_4}}{M_{POC}}\tilde{\rho}_{sed}\, Da(1-\tilde{\phi})\tilde{\alpha}\,\beta - \left(\frac{1+\gamma\tilde{\phi}}{\gamma}\right)\frac{M_{CH_4}\, c_{s,o}}{M_{SO_4}\, c_{m,eqb}} Da_{AOM}\, \tilde{c}_m^l\, \tilde{c}_s^l$$

Sulfate Mass Balance

The sulfate mass balance includes both the reaction pathways for sulfate consumption in which both act as sinks for pore water sulfate and are shown below (Bhatnagar *et al*. 2008).

$$\frac{\partial}{\partial t}[\phi\ \rho_w\, c_s^l] + \frac{\partial}{\partial z}\left[U_f\, \rho_w\, c_s^l\right] = \frac{\partial}{\partial z}\left[\phi\, \rho_w\, D_s \frac{\partial c_s^l}{\partial z}\right]$$
$$- \frac{\phi(1-\phi)}{M_{POC}}\lambda_{POC}(\rho_{sed}\,\alpha)(\rho_w\, c_s^l) - \frac{\phi\ \lambda_{AOM}(\rho_w\, c_m^l)(\rho_w\, c_s^l)}{M_{CH_4}}$$

The reaction terms correspond to sulfate consumption due to POC and AOM, respectively. The dimensionless sulfate mass balance equation is rewritten and presented using the same scaling scheme shown above.

$$\frac{\partial}{\partial \tilde{t}}\left[\left(\frac{1+\gamma\tilde{\phi}}{\gamma}\right)\tilde{c}_s^l\right] + \left(\frac{1+\gamma}{\gamma}\right)(Pe_1 + Pe_2)\frac{\partial \tilde{c}_s^l}{\partial \tilde{z}} = \frac{\partial}{\partial \tilde{z}}\left[\left(\frac{1+\gamma\tilde{\phi}}{\gamma}\right)\frac{D_s}{D_m}\frac{\partial \tilde{c}_s^l}{\partial \tilde{z}}\right]$$
$$- \frac{(1-\tilde{\phi})(1+\gamma\tilde{\phi})}{1+\gamma}\frac{D_s}{D_m}\tilde{\rho}_{sed}\, Da_{POC}\tilde{\alpha}\,\beta\tilde{c}_s^l - \left(\frac{1+\gamma\tilde{\phi}}{\gamma}\right) Da_{AOM}\,\tilde{c}_m^l\,\tilde{c}_s^l$$

DIC Mass Balance

As pointed out previously, DIC mass balance is a necessary step to investigate the competing hypotheses for the loss of sulfate. Similar to the sulfate balance, DIC mass balance not only includes source terms originating from both AOM and POC reactions but also includes source terms like the methanogenesis reaction. In addition to the source terms, the DIC mass balance includes a sink term corresponding to the calcite precipitation reaction as shown below. The sink term originates from the calcium carbonate that precipitates in the reaction. When DIC (or carbonate) reacts with calcium following a 1:1 stoichiometry, both species continue to get consumed and form calcium carbonate which precipitates out of solution as long as the product of calcium and DIC concentration is greater than the solubility product (k_{sp}) of calcium carbonate. When the product of DIC and carbonate concentrations equal the solubility product, their concentrations does not reduce any further, instead precipitates an equivalent amount of calcium carbonate and the reaction reaches equilibrium. The equilibrium reaction is modeled in such a way that calcium concentration is always constrained at the equilibrium concentration. Any calcium which gets consumed in excess of the equilibrium concentration forms calcium carbonate. Consequently, DIC also gets reduced by a similar amount in the reaction. The amount of calcium carbonate generated can be computed from the mass balance equations.

$$\frac{\partial}{\partial t}\left[\phi\ \rho_w\ c_b^l\right] + \frac{\partial}{\partial z}\left[U_f\ \rho_w\ c_b^l\right] = \frac{\partial}{\partial z}\left[\phi\ \rho_w\ D_b\ \frac{\partial c_b^l}{\partial z}\right] + \frac{M_{HCO_3}}{M_{POC}}\rho_{sed}\lambda(1-\phi)\alpha$$

$$+\frac{M_{HCO_3}\ \phi\ \lambda_{AOM}(\rho_w\ c_m^l)(\rho_w\ c_s^l)}{M_{CH_4}M_{SO_4}} + \frac{2M_{HCO_3}\ \phi(1-\phi)\ \lambda_{POC}(\rho_{sed}\ \alpha)(\rho_w\ c_s^l)}{M_{POC}M_{SO_4}} - \ \phi\ \rho_w\ \frac{\Delta c_{CaCO_3}^l}{\Delta t}$$

The reaction terms represent generation of DIC due to methanogenesis, AOM reaction, POC–sulfate reaction, and DIC consumption due to calcite precipitation, respectively. The dimensionless form has been illustrated below using the same scaling scheme discussed above.

$$\frac{\partial}{\partial \tilde{t}}\left[\left(\frac{1+\gamma\tilde{\phi}}{\gamma}\right)\tilde{c}_b^l\right] + \ \left(\frac{1+\gamma}{\gamma}\right)(Pe_1 + Pe_2)\frac{\partial \tilde{c}_b^l}{\partial \tilde{z}} = \frac{\partial}{\partial \tilde{z}}\left[\left(\frac{1+\gamma\tilde{\phi}}{\gamma}\right)\frac{D_b}{D_m}\frac{\partial \tilde{c}_b^l}{\partial \tilde{z}}\right]$$

$$+\ \frac{M_{HCO_3}\ c_{m,eqb}}{M_{POC}\ c_{b,o}}\tilde{\rho}_{sed}Da\left(1-\tilde{\phi}\right)\tilde{\alpha}\ \beta + \left(\frac{1+\gamma\tilde{\phi}}{\gamma}\right)\frac{M_{HCo_3}\ c_{s,o}}{M_{SO_4}\ c_{b,o}}Da_{AOM}\ \tilde{c}_m^l\ \tilde{c}_s^l +$$

$$\frac{2M_{HCo_3}\ c_{s,o}(1-\tilde{\phi})(1+\gamma\tilde{\phi})}{M_{SO_4}\ c_{b,o}(1+\gamma)}\frac{D_s}{D_m}\tilde{\rho}_{sed}\ Da_{POC}\ \tilde{\alpha}\ \beta\tilde{c}_s^l - \left(\frac{1+\gamma\tilde{\phi}}{\gamma}\right)\frac{c_{b,o}}{c_{Ca,o}}\frac{\Delta \tilde{c}_{CaCO_3}^l}{\Delta \tilde{t}}$$

Calcium Mass Balance

Calcium mass balance is another important component including the sink term corresponding to the calcite precipitation reaction and presented as follows. The sink term is represented as the amount of calcium carbonate actually formed in the reaction.

$$\frac{\partial}{\partial t}\left[\phi\ \rho_w\ c_{Ca}^l\right] + \frac{\partial}{\partial z}\left[U_f\ \rho_w\ c_{Ca}^l\right] = \frac{\partial}{\partial z}\left[\phi\ \rho_w\ D_{Ca}\ \frac{\partial c_{Ca}^l}{\partial z}\right] - \ \phi\ \rho_w\ \frac{\Delta c_{CaCO_3}^l}{\Delta t}$$

Using the same scaling scheme developed by Bhatnagar et al., (2007), the dimensionless form is expressed as follows.

$$\frac{\partial}{\partial \tilde{t}}\left[\left(\frac{1+\gamma\tilde{\phi}}{\gamma}\right)\tilde{c}_{Ca}^l\right] + \ \left(\frac{1+\gamma}{\gamma}\right)(Pe_1 + Pe_2)\ \frac{\partial \tilde{c}_{Ca}^l}{\partial \tilde{z}}\ = \frac{\partial}{\partial \tilde{z}}\left[\left(\frac{1+\gamma\tilde{\phi}}{\gamma}\right)\frac{D_{Ca}}{D_m}\frac{\partial \tilde{c}_{Ca}^l}{\partial \tilde{z}}\right] - \ \left(\frac{1+\gamma\tilde{\phi}}{\gamma}\right)\frac{\Delta \tilde{c}_{CaCO_3}^l}{\Delta \tilde{t}}$$

Carbon isotope Mass Balance

Carbon isotope mass balance is also included in our model. A simple carbon mass balance along with its isotope composition for the different species provides an overall conservation of carbon isotopes in the system. Notably, POC, methane, and DIC are the three carbon species with different carbon isotope composition for the various reactions listed above. This motivates us to write the carbon isotope mass balance separately for methane and DIC due to all the reactions sources and sinks in the system as illustrated below. This summarizes the mass conservation for all the species necessary for the mathematical model.

Carbon isotope in Methane

$$\frac{\partial}{\partial t}\left[\phi\,\rho_w\,c_m^l\,\delta^{13}{}_{\mathrm{CH_4}}\right]+\frac{\partial}{\partial z}\left[U_f\,\rho_w\,c_m^l\,\delta^{13}{}_{\mathrm{CH_4}}\right]=\frac{\partial}{\partial z}\left[\phi\,\rho_w\,D_m\frac{\partial(c_m^l\,\delta^{13}{}_{\mathrm{CH_4}})}{\partial z}\right]$$
$$+\frac{M_{CH_4}}{M_{POC}}\rho_{sed}\lambda(1-\phi)\alpha\,\delta^{13}{}_{\mathrm{CH_4,meth}}-\frac{\phi\;\lambda_{AOM}(\rho_w\,c_m^l)(\rho_w\,c_s^l)\delta^{13}{}_{\mathrm{CH_4}}}{M_{SO_4}}$$

The dimensionless mass balance equation is presented as follows.

$$\frac{\partial}{\partial\tilde{t}}\left[\left(\frac{1+\gamma\tilde{\phi}}{\gamma}\right)\tilde{c}_m^l\delta^{13}{}_{\mathrm{CH_4}}\right]+\left(\frac{1+\gamma}{\gamma}\right)(Pe_1+Pe_2)\frac{\partial}{\partial\tilde{z}}\left[\tilde{c}_m^l\,\delta^{13}{}_{\mathrm{CH_4}}\right]=\frac{\partial}{\partial\tilde{z}}\left[\left(\frac{1+\gamma\tilde{\phi}}{\gamma}\right)\frac{\partial(\tilde{c}_m^l\delta^{13}{}_{\mathrm{CH_4}})}{\partial\tilde{z}}\right]$$

$$+\frac{M_{CH_4}}{M_{POC}}\tilde{\rho}_{sed}Da\left(1-\tilde{\phi}\right)\tilde{\alpha}\beta\delta^{13}{}_{\mathrm{CH_4,meth}}-\left(\frac{1+\gamma\tilde{\phi}}{\gamma}\right)\frac{M_{CH_4}\,c_{s,o}\,Da_{AOM}\,\tilde{c}_m^l\,\tilde{c}_s^l\,\delta^{13}{}_{\mathrm{CH_4}}}{M_{SO_4}\,c_{m,eqb}}$$

Carbon isotope in DIC

$$\frac{\partial}{\partial t}\left[\phi\rho_w c_b^l\delta^{13}{}_{\mathrm{HCO_3}}\right]+\frac{\partial}{\partial z}\left[U_f\rho_w c_b^l\delta^{13}{}_{\mathrm{HCO_3}}\right]=\frac{\partial}{\partial z}\left[\phi\rho_w D_b\frac{\partial(c_b^l\delta^{13}{}_{\mathrm{HCO_3}})}{\partial z}\right]$$

$$+\frac{M_{HCO_3}}{M_{POC}}\rho_{sed}\lambda(1-\phi)\alpha\,\delta^{13}{}_{\mathrm{HCO_3,meth}}+\frac{M_{HCO_3}\,\phi\;\lambda_{AOM}\,(\rho_w\,c_m^l)(\rho_w\,c_s^l)\,\delta^{13}{}_{\mathrm{CH_4}}}{M_{CH_4}M_{SO_4}}$$

$$+\frac{2M_{HCO_3}\,\phi(1-\phi)\;\lambda_{POC}(\rho_{sed}\,\alpha)(\rho_w\,c_s^l)\,\delta^{13}{}_{\mathrm{HCO_3,POC}}}{M_{POC}M_{SO_4}}-\phi\rho_w\frac{\Delta(c_{CaCO_3}^l\delta^{13}{}_{\mathrm{HCO_3}})}{\Delta t}$$

The dimensionless form can be represented as follows:

$$\frac{\partial}{\partial\tilde{t}}\left[\left(\frac{1+\gamma\tilde{\phi}}{\gamma}\right)\,\tilde{c}_b^l\,\delta^{13}{}_{\mathrm{HCO_3}}\right]+\left(\frac{1+\gamma}{\gamma}\right)(Pe_1+Pe_2)\frac{\partial}{\partial\tilde{z}}\left[\tilde{c}_b^l\delta^{13}{}_{\mathrm{HCO_3}}\right]$$
$$=\frac{\partial}{\partial\tilde{z}}\left[\left(\frac{1+\gamma\tilde{\phi}}{\gamma}\right)\frac{D_b}{D_m}\frac{\partial\left(\tilde{c}_b^l\,\delta^{13}{}_{\mathrm{HCO_3}}\right)}{\partial\tilde{z}}\right]+\frac{M_{HCO_3}\,c_{m,eqb}\,\tilde{\rho}_{sed}\,Da}{M_{POC}c_{b,o}}\left(1-\tilde{\phi}\right)\tilde{\alpha}\;\beta\;\delta^{13}{}_{\mathrm{HCO_3,meth}}$$
$$+\left(\frac{1+\gamma\tilde{\phi}}{\gamma}\right)\frac{M_{HCo_3}\,c_{s,o}}{M_{SO_4}\,c_{b,o}}Da_{AOM}\,\tilde{c}_m^l\,\tilde{c}_s^l\,\delta^{13}{}_{\mathrm{CH_4}}-\left(\frac{1+\gamma\tilde{\phi}}{\gamma}\right)\frac{c_{b,o}}{c_{Ca,o}}\frac{\Delta(\tilde{c}_{CaCO_3}^l\,\delta^{13}{}_{\mathrm{HCO_3}})}{\Delta\tilde{t}}$$
$$+\frac{2M_{HCo_3}\,c_{s,o}(1-\tilde{\phi})(1+\gamma\tilde{\phi})}{M_{SO_4}\,c_{b,o}(1+\gamma)}\frac{D_s}{D_m}\,\tilde{\rho}_{sed}\,Da_{POC}\,\tilde{\alpha}\,\beta\,\tilde{c}_s^l\,\delta^{13}{}_{\mathrm{HCO_3,POC}}$$

During the AOM reaction, the carbon isotope (δ^{13}) composition in methane and DIC is represented by $\delta^{13}{}_{\mathrm{CH_4}}$. During calcite precipitation, the δ^{13} value in DIC and calcium is $\delta^{13}{}_{\mathrm{HCO_3}}$.

The vertical depth is scaled by the depth of the base of the gas hydrate stability zone (BHSZ) L_t, and is defined as $\tilde{z} = \frac{z}{L_t}$. Time is normalized by a combination of depth of the BSHZ L_t and diffusivity of methane D_m as $\tilde{t} = \frac{t}{{L_t}^2/D_m}$.

The degradable content of POC in the sediment is normalized relative to the initial content deposited at the seafloor (α_o). Normalized organic content in sediment is defined as $\tilde{\alpha} = \frac{\alpha}{\alpha_o}$.

Methane mass fraction in phase i is normalized by methane solubility in the liquid phase at the base of GHSZ ${\tilde{c}^l}_{m,eqb}$, while sulfate, DIC, and calcium mass fractions are normalized by their respective seawater values $c_{s,o}$ (=28 mM), $c_{b,o}$ (=2.29 mM) and $c_{ca,o}$ (=10 mM) to get their corresponding normalized variables. The normalized variables are defined as:

$$\tilde{c}_m^l = \frac{c_m^l}{c_{m,eq}^l} \qquad \tilde{c}_s^l = \frac{c_s^l}{c_{s,o}^l} \qquad \tilde{c}_b^l = \frac{c_b^l}{c_{b,o}^l} \qquad \tilde{c}_b^l = \frac{c_b^l}{c_{b,o}^l}$$

The reduced porosities, $\tilde{\phi}$, $\tilde{\eta}$ and $\tilde{\gamma}$, normalized sediment flux $\widetilde{U}_{sed}$, are defined as:

$$\tilde{\phi} = \frac{\phi-\phi_\infty}{1-\phi_\infty} \qquad \gamma = \frac{1-\phi_\infty}{\phi_\infty} \qquad \eta = \frac{\phi_0-\phi_\infty}{1-\phi_\infty} \qquad \widetilde{U}_{sed} = \frac{U_{sed}}{U_{f,sed}}$$

where the porosity of sediment is ϕ, $\phi_o$is the initial porosity at the seafloor, ϕ_∞ is the minimum porosity attained at greatest depth, and $U_{f,sed}$ is the fluid flux due to sedimentation and compaction. Porosity changes with depth, seafloor porosity $\phi_0 = 0.7$ and minimum porosity attained at greatest depth $\phi_\infty = 0.1$ representing occurrence of compaction.

The fluid flux $U_{f,sed}$ can be defined as a combination of seafloor sedimentation rate $\dot{S}$ and porosities.

$$U_{f,sed} = \frac{1-\phi_o}{1-\phi_\infty}\,\dot{S}\,\phi_\infty$$

The flux of sediment is represented by U_s and is scaled with respect to the fluid flux due to sedimentation $U_{f,sed}$, which equals to a constant, γ.

$$\widetilde{U}_s = \frac{U_s}{U_{f,sed}} = \frac{1-\phi_o}{U_{f,sed}}\,\dot{S} = \frac{\left(\frac{1-\phi_\infty}{\phi_\infty}\right)U_{f,sed}}{U_{f,sed}} = \left(\frac{1-\phi_\infty}{\phi_\infty}\right) = \gamma$$

The numerical model incorporates two fluid fluxes to characterize the compaction driven and external fluid flow relative to diffusion; defined by two independent dimensionless groups known as Peclet numbers. The dimensionless group Peclet number Pe_1 is characterized by the ratio of sedimentation-compaction driven fluid flux to methane diffusion.

$$Pe_1 = \frac{U_{f,sed}\, L_t}{D_m}$$

Similarly, Pe_2 is charaterized by the ratio of external fluid flux from deeper sediments relative to methane diffusion.

$$Pe_2 = \frac{U_{f,ext}\, L_t}{D_m}$$

Crucially, Pe_1 and Pe_2 act in downward and upward directions respectively, and have opposite signs.

The dimensionless group Damkohler number is characterized by the ratio of reaction to diffusion. The three Damkohler numbers for the three main reactions mentioned above are defined as follows

$Da = \frac{\lambda\, L_t^2}{D_m}$	Methanogenesis Reaction
$Da_{AOM} = \frac{\rho_w\, c_{m,eqb}}{M_{CH_4}} \frac{\lambda_{AOM}\, L_t^2}{D_m}$	Anaerobic Oxidation of Methane (AOM)
$Da_{POC} = \frac{\rho_w\, c_{m,eqb}}{M_{POC}} \frac{\lambda_{POC}\, L_t^2}{D_s}$	POC dominated sulfate reduction reaction

All the parameters and dimensionless groups are specified and shown in appendix. To obtain finite solutions, the initial and boundary conditions are specified in addition to the mass balance equations.

Initial Conditions

Organic content, methane, sulfate, DIC, calcium and carbon isotope concentration are assumed to be zero at initial time $\tilde{t} = 0$ for any depth $\tilde{z}$.

$$\tilde{\alpha}(\tilde{z},0) = 0 \qquad \tilde{c}_m^l(\tilde{z},0) = 0 \qquad \tilde{c}_s^l(\tilde{z},0) = \tilde{c}_b^l(\tilde{z},0) = \tilde{c}_{Ca}^l(\tilde{z},0) = 0$$
$$\delta^{13}C_{CH_4}(\tilde{z},0) = 0 \qquad \delta^{13}C_{HCO_3}(\tilde{z},0) = 0$$

Boundary Conditions

Methane is assumed to form biogenically from POC and organic concentration is normalized with the seafloor value, thereby specifying the normalized POC concentration at the seafloor to unity. Methane concentation is normalized relative to the triple point concentration of methane $\tilde{c}_{m,eqb}^l$ at the base of GHSZ. Since, there is no methane at the seafloor, normalized methane concentration at the seafloor is zero. Sulfate, DIC and calcium are normalized with its seawater values and the normalized sulfate, DIC and calcium concentrations are unity at the seafloor. Carbon isotope compostions are

normalized relative to a standard marine carbonate Pee-Dee-Belemnite, therefore the normalized carbon isotope compositions at the seafloor are zero.

$$\tilde{\alpha}(0,\tilde{t}) = 1 \qquad \tilde{c}_m^l(0,\tilde{t}) = 0 \qquad \tilde{c}_s^l(0,\tilde{t}) = \tilde{c}_b^l(0,\tilde{t}) = \tilde{c}_{ca}^l(0,\tilde{t}) = 1$$

$$\delta^{13}C_{CH_4}(0,\tilde{t}) = \delta^{13}C_{HCO_3}(0,\tilde{t}) = 0$$

Upward methane flux is assumed to originate in deeper sediments due to methane generated as a result of methanogenesis. In order to incorporate the upward methane flux, an methane concentration is specified at the base of the simulation domain.

$$\tilde{c}_m^l(0,\tilde{t}) = 0$$

$$\tilde{c}_m^l(\tilde{L}_z,\tilde{t}) = \tilde{c}_{m,ext}^l = \tilde{c}_{m,eqb}^l(\tilde{L}_z)$$

where $\tilde{c}_{m,ext}^l$ is the specified methane concentration at the bottom of the domain L_z, and is equal to the solubility concentration of methane $\tilde{c}_{m,eqb}^l$ at depth L_z. $\tilde{c}_{m,ext}^l$ is also normalized with the triple point concentration of methane.

Similarly, a deep flux of DIC and calcium are specified in the model and therefore an equivalent DIC and calcium molar concentration are specified at the base of the domain whereas sulfate does not have any upward flux in the system. Therefore, zero sulfate concentration and known methane $\tilde{c}_{m,ext}^l$, DIC $\tilde{c}_{b,ext}^l$, and calcium $\tilde{c}_{ca,ext}^l$ concentrations are specified at the base of the simulation domain. During the methanogenesis reaction, equal amounts of methane and DIC are formed, so their molar fluxes are equated at the bottom boundary. DIC molar concentration are specified equal to the molar concentration of methane at the bottom of our simulation domain. For a corresponding DIC concentration, calcium concentration is computed from the solubility product at the bottom boundary. Dirichlet boundary conditions are assumed at the seafloor and bottom of the domain.

$$\tilde{c}_s^l(\tilde{L}_z,\tilde{t}) = \tilde{c}_{s,ext}^l = 0 \qquad \tilde{c}_b^l(\tilde{L}_z,\tilde{t}) = \tilde{c}_{b,ext}^l \qquad \tilde{c}_{ca}^l(\tilde{L}_z,\tilde{t}) = \tilde{c}_{ca,ext}^l$$

where $\tilde{c}_{s,ext}^l$, $\tilde{c}_{b,ext}^l$, and $\tilde{c}_{ca,ext}^l$ are specified concentrations of sulfate, DIC, and calcium at the bottom of the domain $\tilde{L}_z$ normalized with the seawater concentrations $\tilde{c}_{s,o}^l$, $\tilde{c}_{b,o}^l$ and $\tilde{c}_{ca,o}^l$ respectively. Methanogenesis is assumed to occur through CO_2 reduction pathway and follows 70% isotope fractionation (α = 1.07) (Whiticar, 1999). The organic carbon (nominally -25‰) fractionates into lighter methane (~ -60‰) and heavier DIC (~ +10‰) as it gets buried into deeper sediments. The carbon isotope compostions $\delta^{13}C_{CH_4}$ and $\delta^{13}C_{HCO_3}$ in methane and DIC at the bottom boundary are specified based on their fractionated isotope compositions in deeper sediments.

$$\delta^{13}C_{CH_4}(\tilde{L}_z,\tilde{t}) = \delta^{13}C_{CH_4,ext} = -60‰ \qquad \delta^{13}C_{HCO_3}(\tilde{L}_z,\tilde{t}) = \delta^{13}C_{HCO_3,ext} = +10‰$$

Results and discussions

The hyperbolic organic material balance differential equation is numerically solved using an implicit block centered finite difference scheme. To simulate steady state concentration profiles of methane, sulfate, bicarbonate, calcium, carbon isotopes an explicit numerical scheme is formulated and the organic content profile is updated in time. A single point upstream weighting was used to formulate the sediment and fluid advection terms. Steady state methane and sulfate profiles are shown in Figure 6.8.4(a). For close-up view, the profiles are zoomed into and concentration profiles are shown until normalized depth $\tilde{z} = 0.5$ even though the simulated profiles extend till $\tilde{z} = 2$ which is twice the thickness of the hydrate stability zone. With finite Pe_1 (related to burial and sedimentation) and varying external fluid flux (i.e. varying Pe_2), different profiles are plotted corresponding to different SMT depths. On increasing external fluid flux, SMT is observed to be shallower as previously reported by various authors (Borowski *et al.*, 1996; Bhatnagar *et al.*, 2008). Sulfate concentrations are normalized to seafloor values and methane concentrations are normalized to triple point concentration of methane. The arrow indicates increase in external flux. The profiles show that methane concentration increases with depth and on exceeding local solubility concentration, forms hydrates with the excess methane. Thus, methane gets constrained at the saturated value at the top of gas hydrate layer. The methane coming from below is transported towards the seafloor due to diffusive and fluid flux. The fluid flux increases with increase in magnitude of Pe_2 and the methane transports towards the seafloor before it gets constrained at the SMT to zero methane concentration due to the AOM reaction. Near the SMT the diffusion gradients build up and methane profiles tend to bend towards the zero concentration at the SMT.

The sulfate concentrations have the seawater value at the seafloor and when the concentrations are normalized with the seawater value, they attain a unit value at the seafloor $\tilde{z} = 0$. The pore water sulfate is consumed to near-zero concentrations at the SMT by dissolved methane as a result of the AOM reaction. In this work, pore water sulfate consumption has also been modeled to occur through POC driven reduction occuring in the region between the seafloor and the SMT.

In one case, the methane and sulfate profiles constrain the SMT depth to ~8 mbsf ($\tilde{z} = 0.06$) and the top of gas hydrate to ~80 mbsf ($\tilde{z} = 0.6$) matching the real data from site 1244 represented by red curves (Pe_2 = -1.0) in Figure 6.8.4a. The model also computes the DIC, calcium and carbon isotope composition simultaneously with the methane and sulfate concentration profiles. The light blue curves (Figure 6.8.4) represent a case with zero external fluid flux, no AOM, and only POC to consume sulfate in shallow sediments. The red, green and dark blue curves correspond to another case with methanogenesis and AOM reactions, finite fluid flux, but without POC-sulfate reaction. There is a change in slope observed in these profiles at the SMT; which might be explained due to

generation of DIC due to the AOM. In these plots, the DIC concentration is normalized to the seawater concentration, therefore, the normalized DIC concentration is unity at the seafloor.

Calcium present in the system precipitates out in the presence of DIC in shallow sediments forming calcium carbonate. The calcium carbonate formation is the sink for DIC and calcium has been modeled as an equilibrium reaction in this work. Calcium is consumed and finally constrained by the finite equilibrium concentration calculated from the solubility product of calcium carbonate. Increased flux results in increased DIC and reduced pore water calcium resulting in increased authigenic carbonate precipitation. The calcium profiles are normalized to seawater calcium concentration and therefore constrained to unity at the seafloor (Figure 6.8.4c).

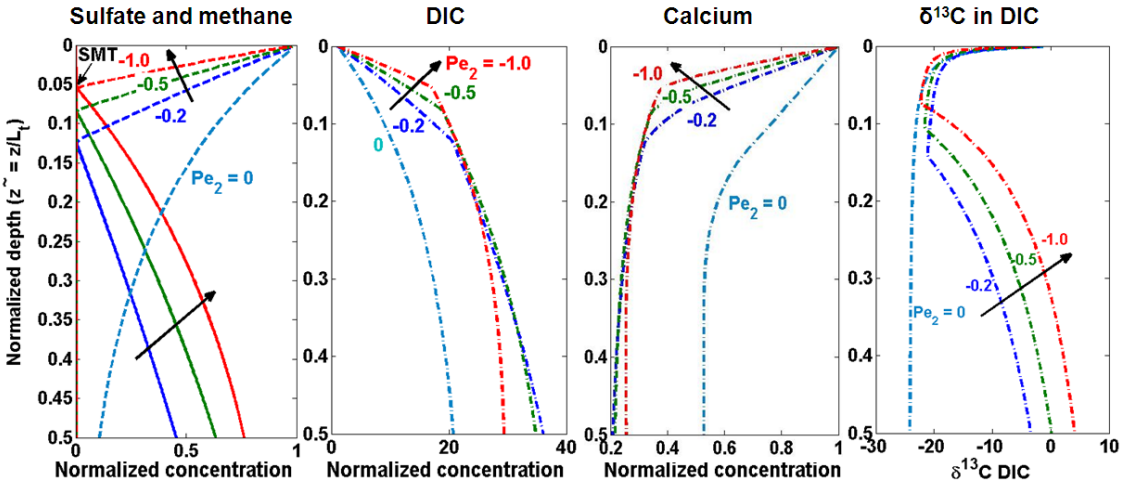

Figure 6.8.4: Normalized concentration profiles at dimensionless time $\tilde{t} = 2.0$. (a) methane, and sulfate, (b) DIC, (c) calcium, (d) $\delta^{13}C$ in DIC. The arrow shows the direction of increasing fluid flux. Parameters: Pe_1=0.04. The light blue curves represent an example of no fluid flux (Pe_2=0), no AOM (Da_{AOM}=0), no methanogenesis (Da=0), with just POC reaction. The red, green and blue curves represent concentration profiles for different fluid fluxes with AOM ($Da_{AOM}=10^8$), POC (Da_{POC}=10) and methanogenesis (Da=0.86) reaction.

The carbon isotope composition $\delta^{13}C$ in DIC is also computed and plotted in Figure 6.8.4d. The normalized carbon isotope in DIC is zero at the seafloor. This reduces to a nominal negative value of -25‰ as a net result of DIC (-60‰) generated at the SMT and a deep bicarbonate (+10‰) source due to methanogenesis in deeper sediments. The $\delta^{13}C$ in DIC value increases with depth below the SMT and finally gets constrained to more positive values since deeper DIC is enriched in ^{13}C as shown in Figure 6.8.4d. The carbon isotope composition in DIC has something very interesting to note. For zero external fluid flux, no methanogenesis, and no AOM, $\delta^{13}C$ in DIC value is -25‰ suggesting dominance of POC reaction. Alternatively, it is observed that with AOM and

methanogenesis, and finite flux, $\delta^{13}C$ in DIC is also - -25‰, as opposed to -60‰ suggested by various authors (Kastner *et al*., 2008). The deep flux of DIC from below of +10‰ mixes with DIC of -60‰ from the AOM reaction at the SMT and brings the carbon isotope composition to a nominal value of -25‰.

From our simulation profiles, the deviation of concentration relative to seawater values is plotted. Similar to the zero external fluid flux interpretation (Only POC, no AOM, no fluid flux), the concentration cross-plot lies on the 2:1 line as shown in red circles in Figure 6.8.5a. The 2:1 concentration cross-plot could also result from a combination of AOM, and methanogenesis with very low fluid flux as shown in blue circles (Figure 6.8.5a). AOM generates 1 mole of DIC and consumes 1 mole of sulfate. On the other hand, methanogenesis generates 1 mole of DIC. Overall, these two reactions form 2 moles of DIC and consume 1 mole of sulfate in the system. In fact, below the SMT, the concentration of DIC increases with no change in sulfate (Figure 6.8.5a).This is due to the DIC flux due to a deep source of DIC as a result of methanogenesis.

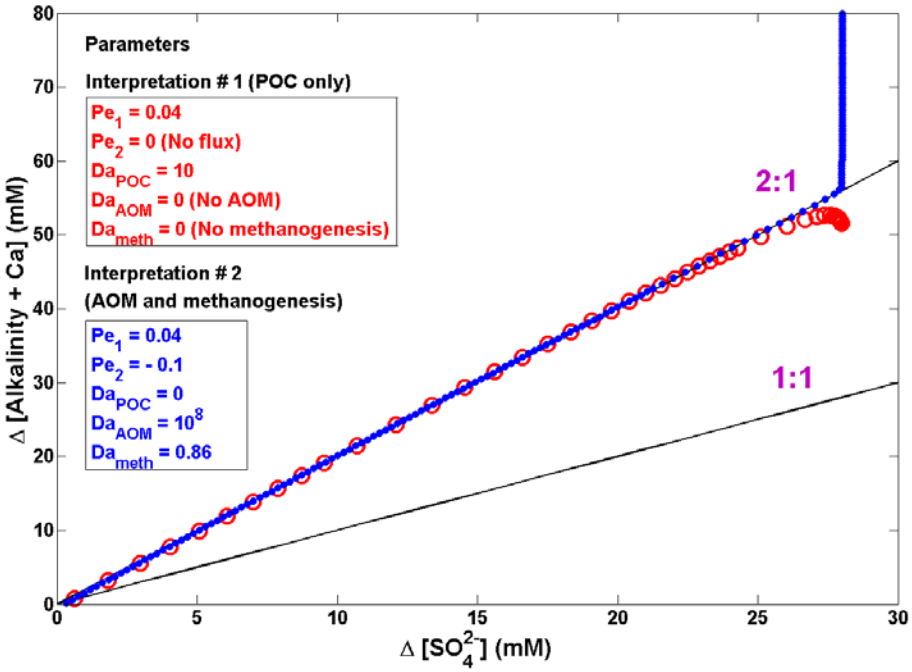

Figure 6.8.5a: Concentration cross-plots for sulfate and DIC relative to seafloor with zero or low upward fluid flux. Parameters: Pe_1=0.04. The red circles represent an example of no fluid flux (Pe_2=0), no AOM (Da_{AOM}=0), no methanogenesis (Da=0), with just POC reaction (Da_{POC}=10). The blue curve represents an example of low finite flux (Pe_2=-0.1), with AOM ($Da_{AOM}=10^8$), methanogenesis (Da=0.86), but no POC (Da_{POC}=0) reaction. 2:1 correspondence could not only be achieved by POC alone, but also by a combined effect of AOM and methanogenesis.

Therefore, 2:1 slope for DIC and sulfate concentration cross-plot does not necessarily suggest POC driven sulfate consumption reaction. It could also result

from combinations of AOM and a deep bicarbonate source (methanogenesis) and fluid flux.

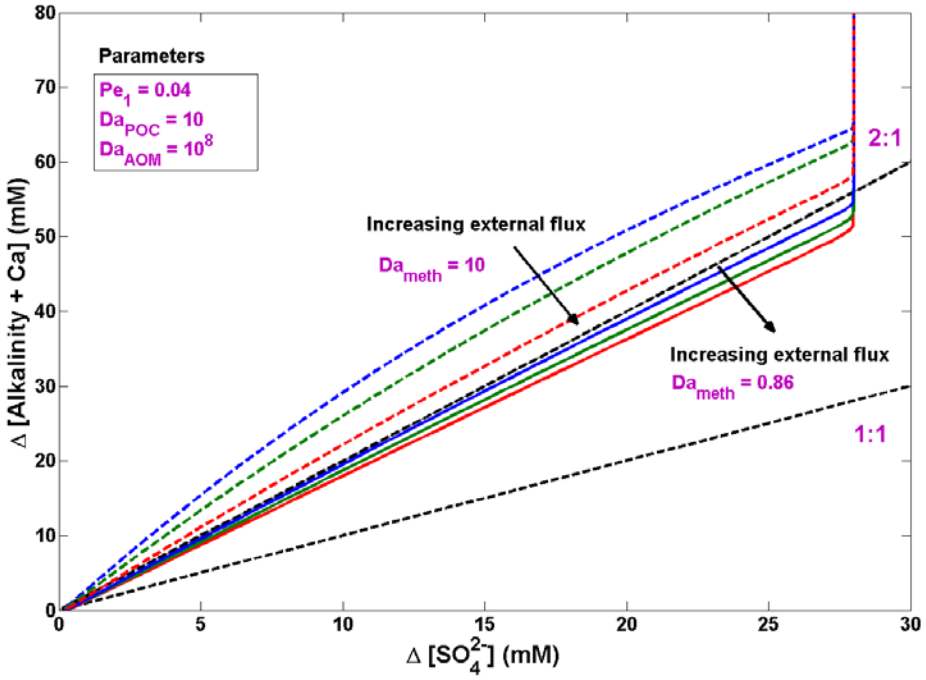

Figure 6.8.5b: Concentration cross-plots for sulfate and DIC relative to seafloor with finite flux and rate of methanogenesis. Parameters: Pe_1=0.04, Da_{AOM}=10^8, Da_{POC}=10. The bold curves represent lower rate of methanogenesis, Da=0.86 and dashed curves correspond to a higher rate Da=10. On increasing fluid flux the slope of the cross-plot decreases. Higher rate of methanogenesis results in more DIC generation hence the curves are shifted with an increased slope.

On increasing the external fluid flux, the slope of the concentration cross-plots decreases (Figure 6.8.5b). On increasing the rate of methanogenesis, the slope of the concentration cross-plots increases. This increase is because more of DIC is generated with increased methanogenesis (Figure 6.8.5b).

From the computed concentration profiles, gradients are calculated and the diffusive fluxes of DIC and methane relative to sulfate diffusive fluxes at the SMT are plotted in Figure 6.8.6. The red markers represent DIC and blue correspond to methane. Both methane and DIC fluxes show 1:1 correspondence with the sulfate fluxes. This is obviously due to the AOM at the SMT as reported by several authors in the past (Borowski *et al*., 1996). Even on increasing the rate for POC reaction from zero to 10 does not shift the flux cross-plot from 1:1 line. Squares (Da_{POC}=10) and circles (Da_{POC}=0) show the two different rates for POC reaction. Notably, that the net DIC flux at the SMT is calculated as a difference in flux coming from deeper sediments and shallow flux going towards the seafloor.

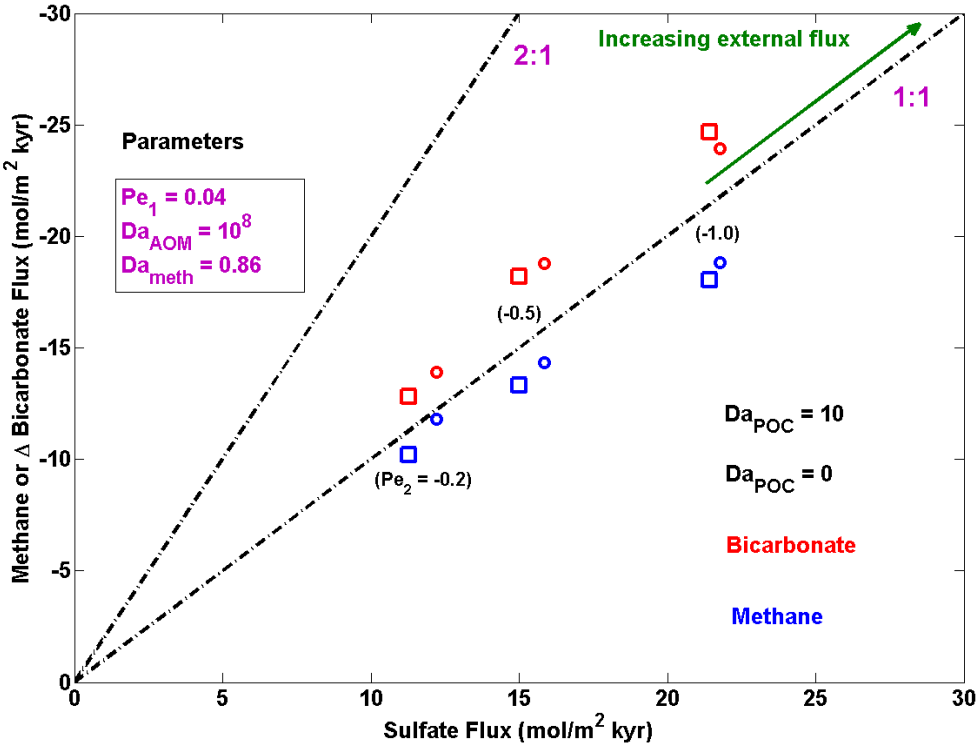

Figure 6.8.6: Flux cross-plots of methane (blue) versus sulfate or DIC (red) versus sulfate across the SMT showing 1:1 correspondence for AOM dominated system. Squares (Da_{POC}=10) and circles (Da_{POC}=0) show the two different rates for POC reaction. Changing the rate of POC reaction does not alter the flux correspond of the above species.

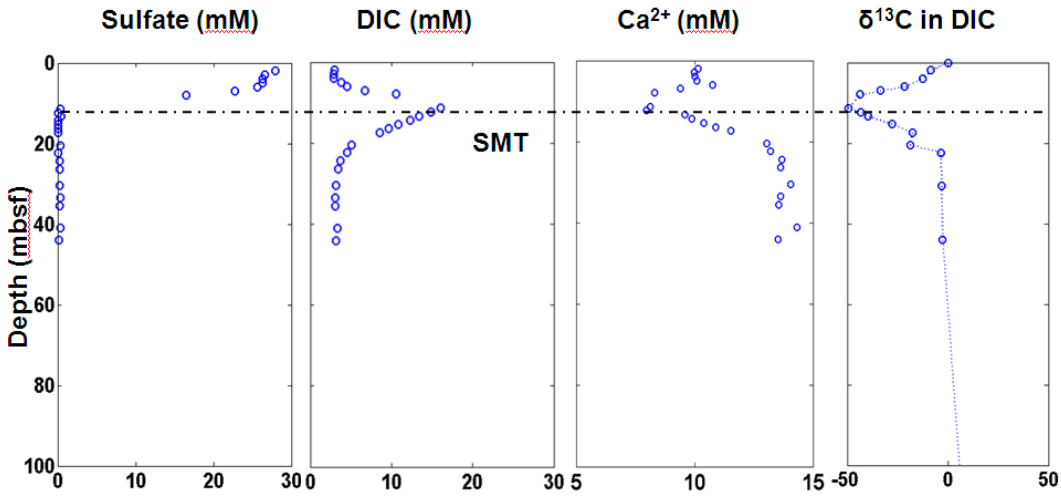

Figure 6.8.7: Sulfate, methane, alkalinity (DIC), calcium concentration profiles and carbon isotope $\delta^{13}C$ composition in DIC for shallow sediment at site KC151 on Gulf of Mexico (original data from Kastner *et al.*, 2008)

Example site – Gulf of Mexico Keathley Canyon 151

A second example site is simulated from the Gulf of Mexico Keathley Canyon 151 where DIC is the limiting species and calcium is in excess as shown in observed data (Figure 6.8.7). Due to high calcium concentration, DIC gets consumed in deeper sediments. There exists a change in slope at the SMT in the profiles shown in Figure 6.8.7. The DIC concentration increases in the region between the seafloor and the SMT but drops below the SMT. With the help of the numerical model, the concentration profiles were simulated for site KC151 for a given set of parameters (see appendix). From the simulated concentration profiles, the change in DIC and sulfate concentration was cross-plotted, with respect to seawater values as shown in Figure 6.8.8. The concentration cross-plot lie away from the 2:1 line (closer to 1:1 line) and in fact, on increasing the external fluid flux the slope of the cross-plot decreases, similar to what was found at Hydrate Ridge site example (Figure 6.8.5b).

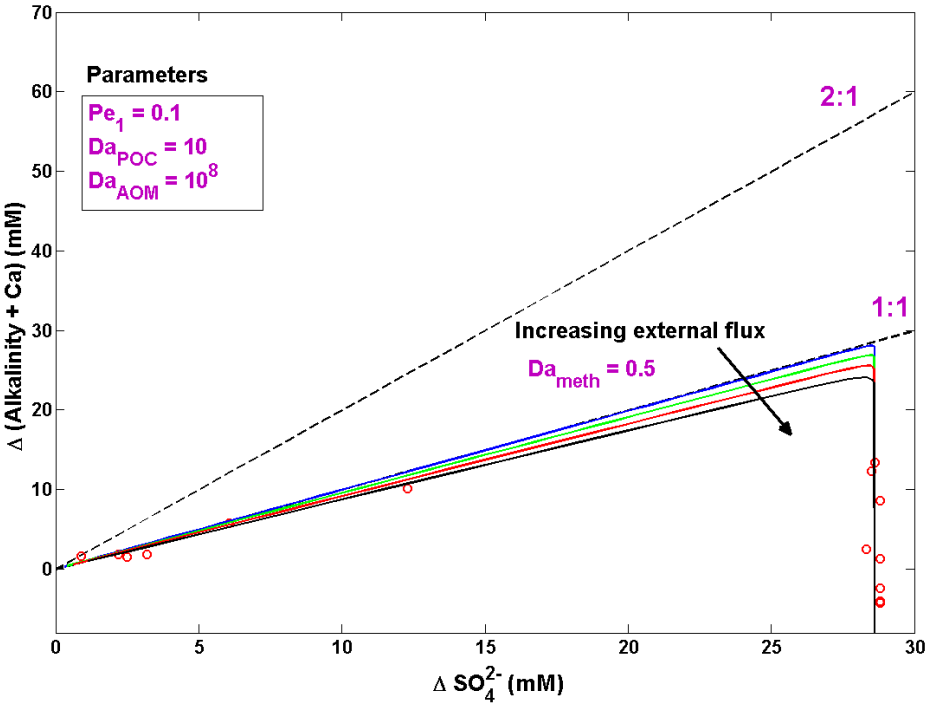

Figure 6.8.8: Concentration cross-plots for sulfate and DIC relative to seafloor with finite flux and rate of methanogenesis. Parameters: Pe_1=0.05, Da_{AOM}=10^8, Da_{POC}=10, Da=0.5. The bold curves represent concentration cross-plots for Gulf of Mexico, Keathley Canyon KC151. On increasing fluid flux, the slope of the bold curves decreases. Note that the concentration of DIC drops below the SMT because calcium consumes the DIC at greater depths. Therefore, the concentration cross-plot slope is significantly lower than 2:1.

Conclusions

The modeling shows us that a 2:1 correspondence in concentration cross-plot for alkalinity and sulfate is not limited to POC driven sulfate reduction. The 2:1 concentration cross-plot could also result from combinations of AOM, methanogenesis, and fluid flux.

On increasing the external fluid flux the slope of the concentration cross-plot decreases. Higher rate of methanogenesis results in more DIC generation hence the curves are shifted with an increased slope. A trade-off of fluid fluxes and rate of methanogenesis decides whether the concentration cross-plot lies on 2:1 or not.

The $\delta^{13}C$ values in DIC are significantly more positive than -60‰ (e.g. -22‰) and can result from the combined input of AOM and a deep bicarbonate source (from methanogenesis).

Flux cross-plot of methane versus sulfate or DIC versus sulfate across the SMT lie on the 1:1 slope, if dominated by AOM. For AOM dominated systems, the SMT depth can be used as a proxy to determine the upward methane flux above marine gas hydrate sediments.

References

Berner, R. A. (1980), *Early Diagenesis: A Theoretical Approach*, Princeton Univ. Press, 213 Princeton, NJ

Bhatnagar, G., Chatterjee, S., Chapman, W. G., Dickens, G. R., Dugan, B., and Hirasaki, G. J. (2010), Analytical theory for relating depth of the sulfate-methane transition to gas hydrate saturation (in preparation), to be submitted to *Geochemistry, Geophysics, Geosystems*

Bhatnagar, G., Chapman, W. G., Dickens, G. R., Dugan, B., and Hirasaki, G. J. (2008), *Sulfate-methane transition as a proxy for average methane hydrate saturation in marine sediments*, *Geophys. Res. Lett.*, 35, L03611, doi:10.1029/2007GL032500

Bhatnagar, G., Chapman, W.G., Dickens, G.R., Dugan, B. and Hirasaki, G.J. (2007), *Generalization of gas hydrate distribution and saturation in marine sediments by scaling of thermodynamic and transport processes*, *Am. J. Sci*., 307: p 861-900

Boudreau, B. P., and J. T. Westrich (1984), *The dependence of bacterial sulfate reduction on sulfate concentration in marine sediments*, *Geochim. Cosmochim. Acta*, *48*, 2503-2516

Borowski, W. S., Paull, C. K., and Ussler III, W. (1999) *Global and local variations of interstitial sulfate gradients in deep-water, continental margin sediments: Sensitivity to underlying methane and gas hydrates*, *Mar. Geol.*, 159:131–154

Borowski, W. S., C. K. Paull, and W. Ussler III (1996), *Marine pore-water sulfate profiles indicate in situ methane flux from underlying gas hydrate*, *Geology*, *24(7)*, 219 655-658

Buffett, B. A. and Archer, D. (2004), *Global inventory of methane clathrate: Sensitivity to changes in the deep ocean*, *Earth Planet. Sci. Lett.*, 227:185–199

Davie, M. K. and Buffett, B. A. (2001), *A numerical model for the formation of gas hydrate below the seafloor*, *J. Geophys. Res.*, 106:497–514

Dickens, G.R., Snyder, G. (2009), *Interpreting upward methane flux*, *Fire in the Ice*, Winter, p 7-10

Dickens, G. R. (2001), *The potential volume of oceanic methane hydrates with variable external conditions*, *Org. Geochem.*, 32:11791193

Kastner, M., Torres, M., Solomon, E., and Spivack, A. J. (2008), *Marine pore fluid profiles of dissolved sulfate: do they reflect in situ methane fluxes*? *Fire in the Ice*, Summer, p 6-8

Li, Y., and Gregory, S., 1974, Diffusion of ions in sea water and in deep-sea sediments: Geochimica et Cosmochimica Acta, v. 38: 703–714

Paull, C. K., W. Ussler III, T. Lorenson, W. Winters, and J. Dougherty (2005), *Geochemical constraints on the distribution of gas hydrates in the Gulf of Mexico*, *Geo. Mar. Lett.*, *25*: 273-280

Tréhu, A. M., Long, P. E., Torres, M. E., Bohrmann, G., Rack, F. R., Collett, T. S., *et al*., (2004), *Three-dimensional distribution of gas hydrate beneath southern Hydrate Ridge: Constraints from ODP Leg 204, Earth Planet. Sci. Lett.*, 222: 845–862

Tréhu A. M., Bohrmann G., Rack F. R., Torres M. E., *et al*., (2003), *Proc, ODP, Init. Repts.*, vol. 204; College Station, TX (Ocean Drilling Program), 1–132 doi:10.2973/odp.proc.ir.204.103.2003

Whiticar M., J., (1999), Carbon and hydrogen isotope systematics of bacterial formation and oxidation of methane, *Chemical Geology,* 161: 291–314

Appendix – Notations

$c_i^j, \tilde{c}_i^j$	Mass fraction of component i and corresponding normalized value in phase j
$c_{m,eqb}$	Methane mass fraction in pore water at the base of gas hydrate stability zone (BHSZ)
D_m, D_s, D_b, D_{Ca}	Diffusivities of methane, sulfate, DIC, and calcium
Da_{AOM}, Da_{POC}, Da	Damkohler number for AOM, POC and

	methanogenesis reactions
L_t, L_s	Depth to base of GHSZ, Depth to SMT
$M_{CH_4}, M_{SO_4}, M_{HCO_3}, M_{Ca}, M_{POC}$	Molecular weight of methane, sulfate, DIC, calcium, and POC, respectively
Pe_1, Pe_2	Peclet numbers for compaction driven and external fluid flow
$t, \tilde{t}$	Dimensional time and dimensionless time, respectively
U_f, U_s	Net fluid flux and sediment flux, respectively
$\widetilde{U}_f, \widetilde{U}_s$	Dimensionless net fluid flux and sediment flux, respectively
$U_{f,sed}, U_{f,ext}$	Fluid flux due to sedimentation-compaction and upward external flow, respectively
v_s	Sediment velocity
$z, \tilde{z}$	Vertical depth and normalized vertical depth, respectively
$\alpha, \tilde{\alpha}$	Organic content in sediment and normalized value, respectively
α_o, β	Organic content in seafloor and normalized value, respectively
$\delta^{13}{}_{CH_4}, \delta^{13}{}_{HCO_3}$	$\delta^{13}C$ value in methane and DIC, respectively
$\delta^{13}{}_{CH_4,meth}$	$\delta^{13}C$ composition in methane in methanogenesis reaction
$\delta^{13}{}_{HCO_3,meth}, \delta^{13}{}_{HCO_3,POC}$	$\delta^{13}C$ composition in DIC for methanogenesis and POC driven sulfate consumption reaction, respectively
$\phi, \tilde{\phi}$	Sediment porosity and reduced sediment porosity, respectively
ϕ_o, ϕ_∞	Sediment porosity at seafloor and minimum porosity at depth, respectively
γ, η	Reduced porosity parameters
$\lambda, \lambda_{AOM}, \lambda_{POC}$	Rate of methanogenesis, AOM and POC driven

	sulfate consumption
ρ_i , $\tilde{\rho}_i$	density of the phase i and normalized value, respectively

Subscripts and superscripts

$m, s, b, Ca, CaCO_3, w, sed$	methane, sulfate, DIC, calcium, calcium carbonate, water and sediment components, respectively
l	liquid phase

Model parameters	**Hydrate Ridge 1244**	**Gulf of Mexico KC151**
Seafloor depth (m)	890	1300
Seafloor temperature (℃)	3.8	4
Geothermal gradient ($℃/m$)	0.061	0.038
Depth to GHSZ: L_t (mbsf)	133.4	316.5
Depth to SMT: L_s (mbsf)	8.5	9
Methane solubility at base of GHSZ: $c_{m,eqb}$	1.701×10^{-3}	2.11×10^{-3}
Sedimentation rate: $\dot{S}$ (cm/kyr)	27	25
Methane diffusivity: D_m (m^2/s)	0.87×10^{-9}	
Sulfate diffusivity: D_s (m^2/s)	0.56×10^{-9}	
DIC diffusivity: D_b (m^2/s)	0.60×10^{-9}	
Calcium diffusivity: D_{Ca} (m^2/s)	0.40×10^{-9}	
Rate of methanogenesis:	5×10^{-14}	
Fluid flux due to sedimentation: $U_{f,sed}$(m/s)	2.85×10^{-13}	2.64×10^{-13}
Normalized sediment density $\tilde{\rho}_{sed} = \rho_{sed}/\rho_w$	2.57	
TOC: α_o(%)	1.5	0.5
$Pe_1 = \frac{U_{f,sed} L_t}{D_m}$	0.04	0.1
$Pe_2 = \frac{U_{f,ext} L_t}{D_m}$	-0.2, -0.5, -1.0	-1.0, -2.0, -5.0

$Da_{POC} = \frac{\rho_w c_{m,eqb}}{M_{POC}} \frac{\lambda_{POC} L_t^2}{D_s}$	10	
$Da_{AOM} = \frac{\rho_w c_{m,eqb}}{M_{CH_4}} \frac{\lambda_{AOM} L_t^2}{D_m}$	10^8	
$Da = \frac{\lambda L_t^2}{D_m}$	0.86	0.5
$\beta = \frac{(3/4)\alpha_o}{c_{m,eqb}}$	2.2	0.59

Task 7: Analysis of Production Strategy

J. Phirani & K. K. Mohanty, University of Texas at Austin

Abstract

A large deposit of gas hydrate is found in the Gulf of Mexico (GOM) block AC 818. In the last 6 months, we have worked on assessing the production from this block using a thermal, compositional, 3-D simulator in equilibrium mode. Four components (water, methane, hydrate and salt) and four phases (gas, aqueous-phase, hydrate and ice) are considered where salt is assumed to be in aqueous phase only. The reservoir GOM, block AC 818 is reported to be an unconfined reservoir. For these types of reservoirs, depressurization is ineffective and warm water flooding is necessary for production. We study different well configurations for production from this hydrate reservoir using warm water flooding. Vertical wells, horizontal wells and a combination of both are considered. Horizontal wells increase the area of sweep by warm water in hydrate bearing sediments and increase the gas production to 48% of original gas in place as compared to 15% produced by using vertical wells. Positions of horizontal wells with respect to the aquifer also play an important role in production.

Reservoir description

The block AC 818 that is considered in this work is a 1200m long and 500m wide reservoir, as shown in Figure 1. It has a 18m thick hydrate layer which is underlain by an infinite aquifer. In the hydrate zone, hydrate saturation is 0.75 and water saturation is 0.25. Initial pressure at the bottom of the reservoir is 31.4MPa and initial temperature is 294.88K which vary in the reservoir according to hydrostatic pressure drop and geothermal gradient, respectively. To model the infinite aquifer a 12m thick aquifer zone is considered for simulation in which the bottom most 3m layer was assumed to have a permeability $1/10^{th}$ of the hydrate layer absolute permeability. The water saturation is 1.0 for the aquifer layer. For over-burden, no mass flow is allowed while heat can transfer with a specified heat transfer coefficient. At the under-burden, we have an infinite aquifer, so, heat transfer is allowed and the pressure is specified at the bottom boundary. The water can come into the reservoir or go out according to the pressure difference between the bottom most grid layer and the boundary pressure. For lateral boundaries no heat or mass flow is considered, due to symmetry.

Different well configurations (Figures 1b-g) considered for production from this reservoir are described below:

1. Vertical wells: It is assumed that the reservoir will be developed in a 5-spot pattern and a quarter of a 5-spot pattern is studied. The reservoir is discretized by 50 x 25 x 10 gridlocks.
2. Horizontal wells: Horizontal injectors and producers are considered along the length which are 250m apart. Different positions for horizontal wells are considered.

3. Vertical injector and horizontal producer: The gas dissociated from hydrates rises due to gravity. So, a horizontal production well is considered at the top of the hydrate layer while a vertical injector is placed at the corner of the reservoir, as shown in the figure. The reservoir is discretized by 25 x 12 x 10 gridlocks.
4. Vertical producer and horizontal injector: The injected water drains down due to gravity. So, a horizontal injector at the top of the reservoir and a vertical producer at the corner are considered, as shown in the figure.

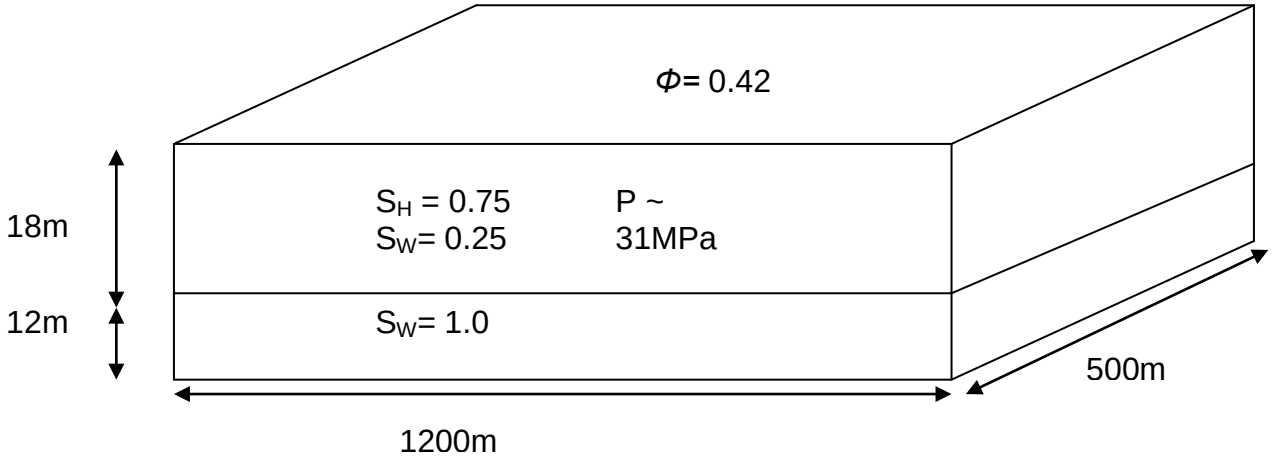

Figure 1a: Reservoir description considered for production

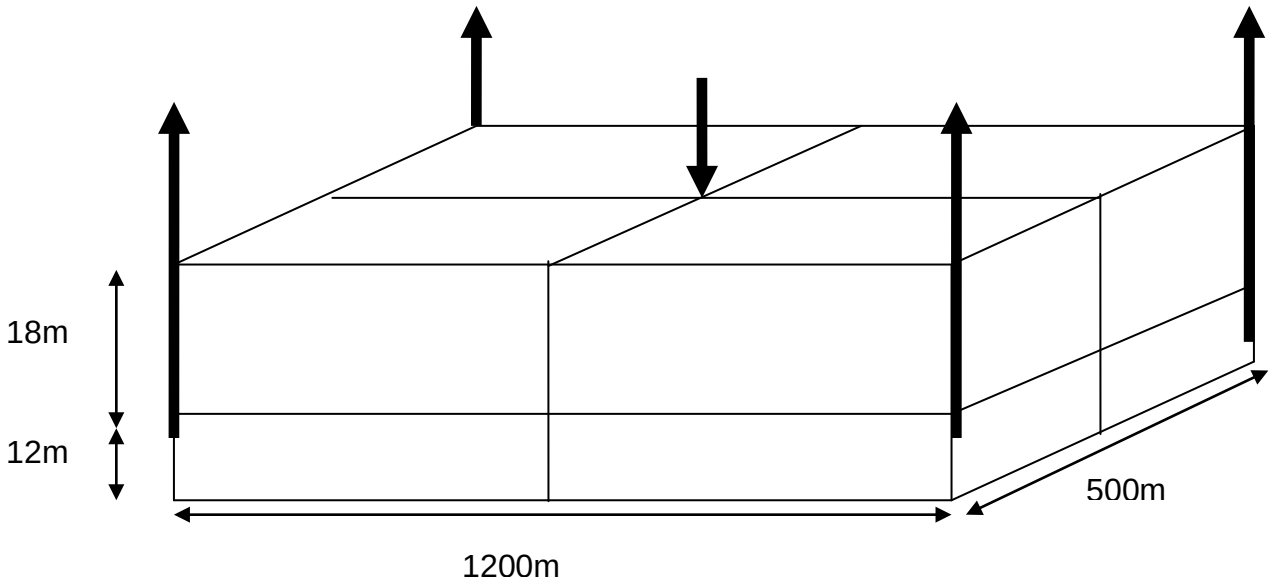

Figure 1b: Reservoir developed in 5-spot pattern

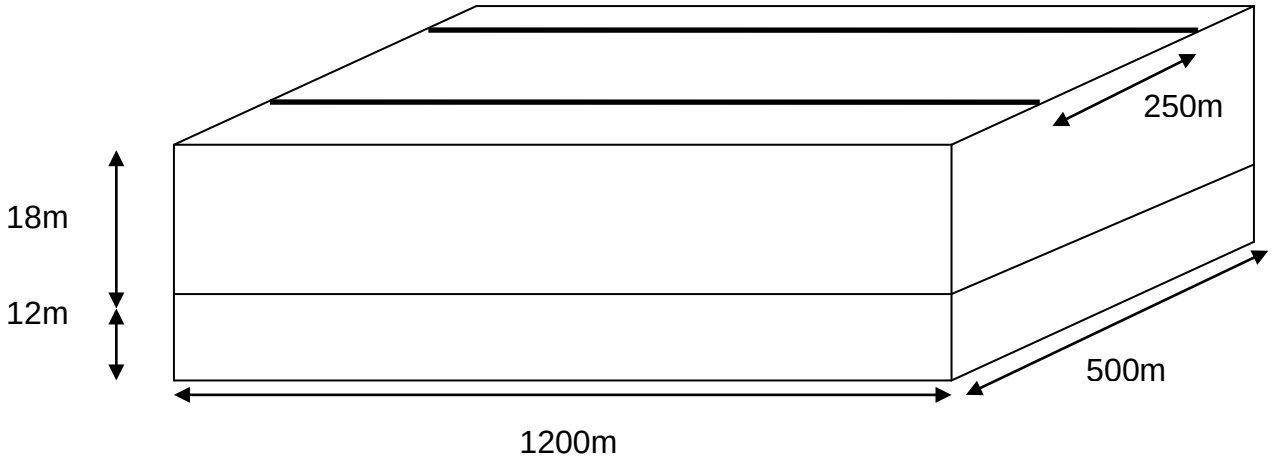

Figure 1c: Reservoir with horizontal wells at the top

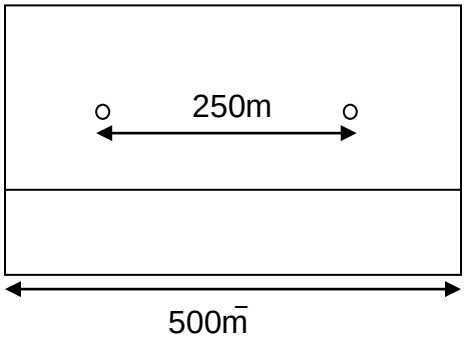

Figure 1d: Reservoir with horizontal wells in the middle of hydrate bearing layer

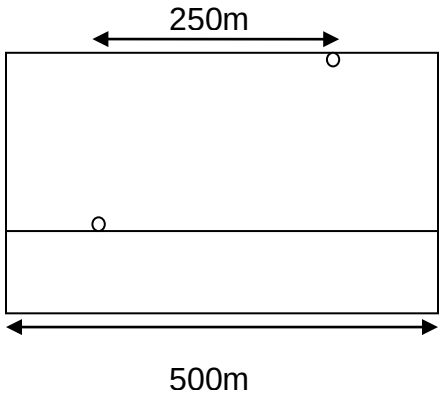

Figure 1e: Reservoir with injector at bottom of hydrate bearing layer and producer at top

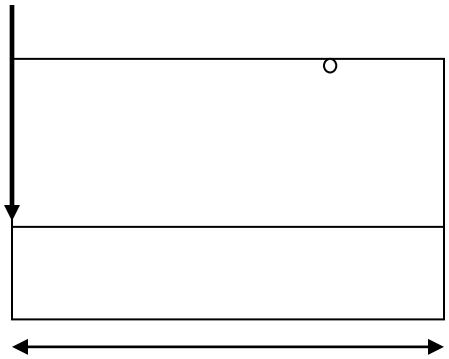

Figure 1f: Reservoir showing face perpendicular to producer and along the injector on left

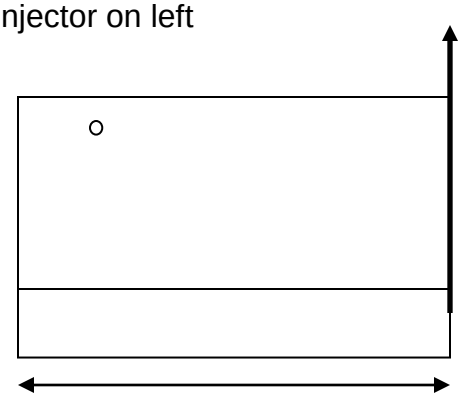

Figure 1g: Reservoir showing face perpendicular to injector and along the producer on right

Results

Figure 2 shows the production as a percentage of the original gas in place for different well configurations. For all the well configurations, the well temperature and pressure conditions are kept the same. The injection well injects water at 50°C and at a pressure of 50MPa. The producer well pressure is maintained at 4 MPa. With a five spot pattern (Figure 1b), the total production is similar to the warm water flooding of an unconfined reservoir, as shown by Phirani et al. (2009), even though the reservoir, injection and production conditions are entirely different. We are able to produce about 15% of the original gas in place when the vertical wells penetrate or do not penetrate the aquifer layer as shown by 'vertical_wells' and 'short_vertical_wells', respectively. We are able to produce more gas when horizontal wells are used. Different configurations for horizontal wells are used. In hydrate reservoir, for warm water injection we inject water and produce gas. The water drains down due to gravity and gas rises up due to gravity. So the first case we study is with both the injector and producer wells on the top of hydrate bearing zone, shown by 'horizontal_wells_top'. The horizontal wells are 1200m long and are located in the 3rd grid block layer from the

longitudinal sides, as shown in Figure 1c. The production curve shows that the gas production in the first 700 days is negligible; so different positions of the horizontal wells are studied. The case 'horizontal_wells_mid' shows the production curve (Figure 3) when both the horizontal wells in the middle of the hydrate bearing zone (Figure 1d). In this case the production begins a little earlier than the previous case. Though we are injecting water, because the temperature of injection water is more than reservoir temperature, the water injected also rises due to the density difference. So we simulate the case where the production well is at the top of hydrate bearing zone while the injection well is below the hydrate bearing zone, as shown by 'producer_up_injector_down'. Figure 1e shows the position of the wells for this case. In this case we are able to produce from the beginning but the final gas production is similar to the previous cases with about 47% of OGIP produced. If we increase the distance between the horizontal wells and the wells are located on the extremes, then the production rate and total production decreases as shown in the case 'producer_up_injector_down_onsides'.

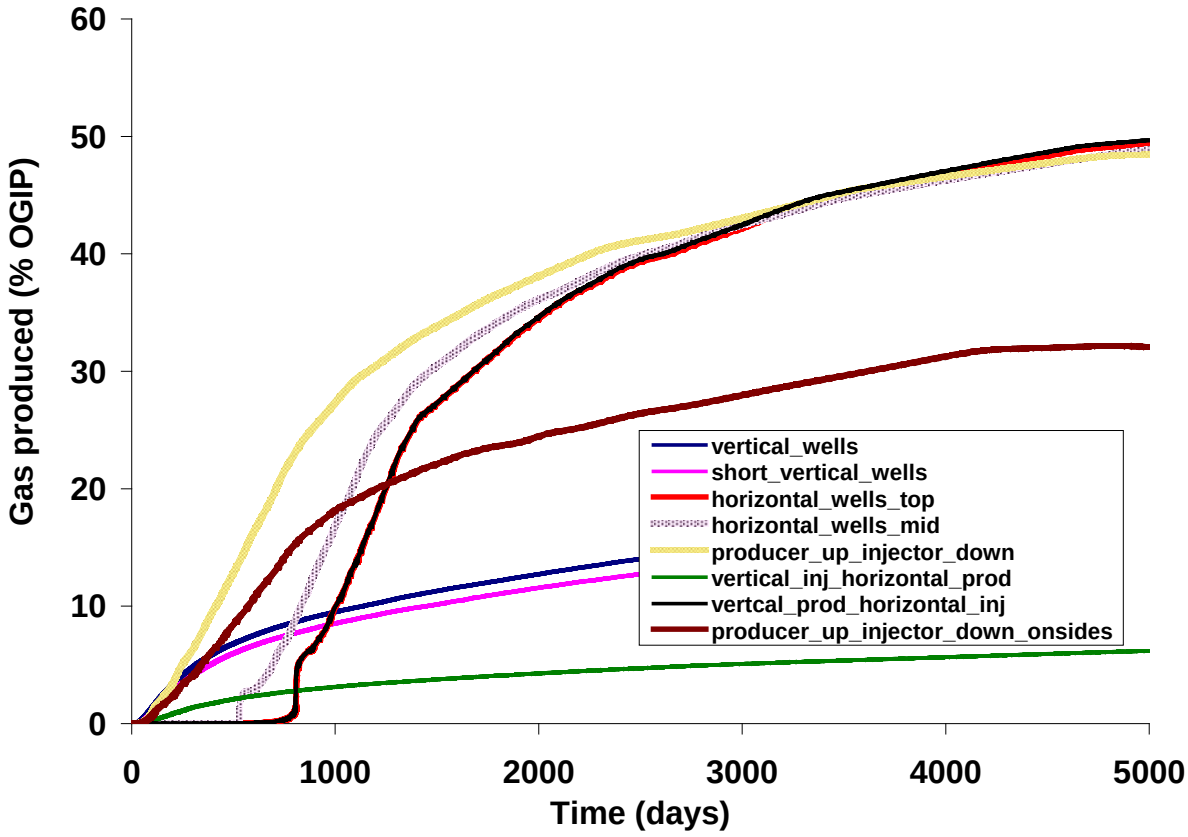

Figure 2: Production curves for different well configurations

Two more cases are studied where a combination of vertical and horizontal wells is considered. The production curve for 'vertical injector and horizontal producer' is shown by 'vertical_inj_horizontal_prod'. The total production for this case is

least of all the cases. But when we have horizontal injector and vertical producer shown by ‘vertical_prod_horizontal_inj’ the production curve is similar to the horizontal well case.

Vertical Wells

When both wells are vertical, we consider a 5-spot pattern in the reservoir, as shown in Figure 1b and simulate a quarter of the pattern. In the simulation domain, we have one injection and one production well in the reservoir. We simulate two cases of the 5-spot pattern. In one case, the vertical wells penetrate the aquifer zone (‘vertical_wells’ in Figure 2) and in another, they do not penetrate the aquifer zone (‘short_vertical_wells’ in Figure 2). We are able to produce about 18% of the OGIP. This is because both the vertical wells are connected to the infinite aquifer and water flow is easier in the aquifer as compared to hydrate bearing layer because the presence of hydrates reduces the permeability. The easier water flow helps in warm water convection in the first case and the production is a little higher than the second case. But after about 500 days most of the water goes into the infinite aquifer and horizontal sweep of warm water slows down.

Horizontal wells

Injector and producer at the top

Figure 2 shows that we can get about 48% of OGIP if we use horizontal wells. Different configurations of horizontal wells are studied. Figure 1c shows the position of the horizontal wells when both the wells are at the top. The production curve for this configuration is shown in Figure 1 as ‘horizontal_wells_top’. Before 700 days, the production as shown in Figure 2 is negligible. This is because the injector is in hydrate bearing low permeability zone. This decreases the injectivity of warm water in the system and initial heating of the reservoir happens by only conduction. After some of the hydrates near the well region dissociate, the convection of warm water becomes easy and hydrate dissociation rate increases.

Horizontal wells in the middle

To increase the initial production, we move the horizontal wells near the aquifer layer to the middle of the hydrate bearing zone (Figure 1d). The production curve for this case is shown by ‘horizontal_wells_mid’. The production in this case starts at about 500 days. Injection water is lighter than the water present in the reservoir and hence water rises; final production of gas is again about 48% of OGIP. As the warm water rises due to gravity, we can use injection well at the bottom of the hydrate bearing layer and producer at the top as gas also rises due to gravity.

Injector at bottom-producer at top

Figure 1e shows the face of the reservoir perpendicular to the horizontal wells for this case. In this case the injection well is near the infinite aquifer which makes the warm water flow easy. Figure 2 shows that we are able to produce significant amount of gas from the beginning but the final production is about 48% of OGIP (case 'producer_up_injector_down').

The final production is similar in all the cases of horizontal wells. The total production is governed by the hydrate bearing area that warm water is able to sweep, which depends on horizontal convection of warm water. In all the cases this is similar. We also study the production from combinations of vertical and horizontal wells, which includes two cases: vertical injector-horizontal producer and vertical producer-horizontal injector.

Vertical and Horizontal Wells

Vertical injector-horizontal producer

Figure 1f shows the face perpendicular to the horizontal well when we have a vertical injector and a horizontal producer. In this case, we have a horizontal producer, which tries to depressurize the reservoir at 4MPa and the producer is not directly connected to the infinite aquifer. The injector injects water at 50C at a pressure of 50MPa. The initial hydrate saturation is 0.75, which is very high and decreases the permeability of hydrate bearing zone to a great extent. This reduces the water productivity of the horizontal well and the pressure does not drop to gas stable zone even in the near well regions. The production well is at the top of hydrate bearing layer about 120m from the right side. In this case warm water can not reach faces away from the vertical injection well leading to low gas production as shown in Figure 2. Another reason of low production in this case is that the wells are not aligned as in the case of two vertical wells where pressure drop along the wells help in horizontal convection of the warm water. The total gas production in this case is less than 10% of OGIP.

Vertical producer-horizontal injector

Figure 2 shows that for this case 'vertical_prod_horizontal_inj', the production curve is similar to that of the horizontal wells at top. In this case, we have injector at the top, as shown in Figure 1. This is because most of the production is due to the thermal stimulation by warm water. With a horizontal injection well, we are able to sweep the same area of the reservoir.

Sensitivity to distance between the horizontal wells

If the horizontal wells are on the extreme ends of the reservoir, i.e., we increase the distance between the wells. Figure 2 case

‘producer_up_injector_down_onsides’ shows that the total production decreases as the area swept by the wells decrease. We compare the case ‘producer_up_injector_down’.

Effect of Salt Content

We simulate the reservoir with initial salt content of 1% while injecting fresh water. Figure 3 shows the production profile for this case and compares it with no salt case. This shows that the salt content increases the gas production very little and can be neglected. One reason for this can be that the hydrate dissociation produces fresh water and decrease the effective salt concentration in the reservoir leading to less difference between the two cases.

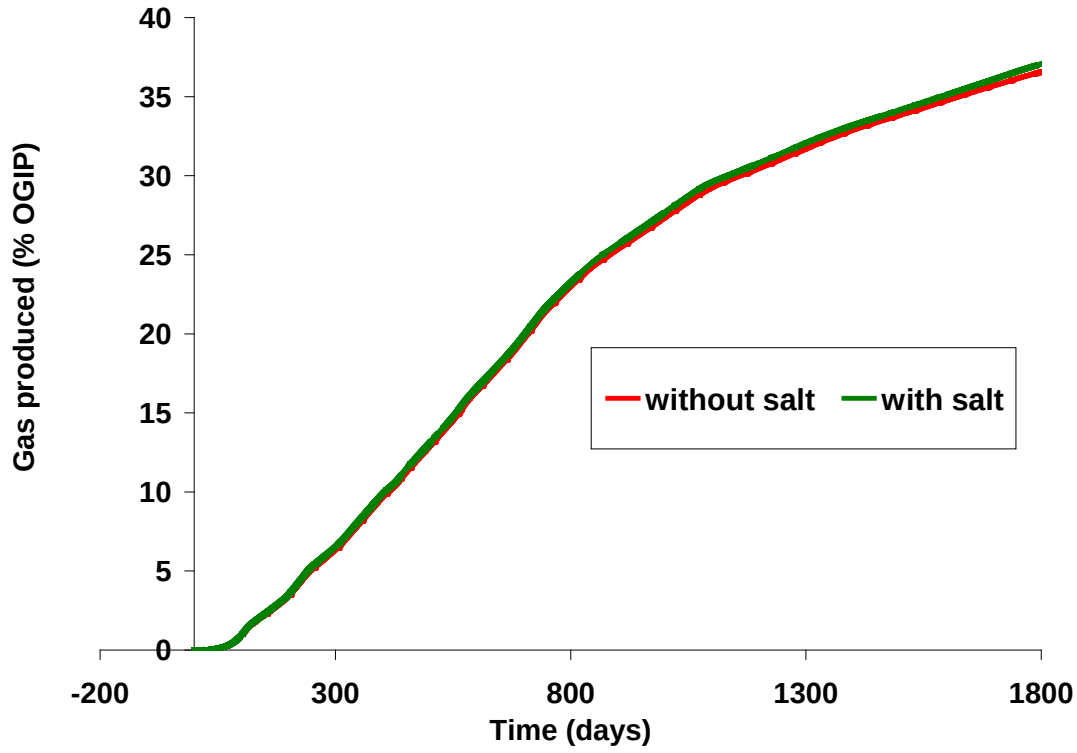

Figure 3: Comparison of production curve for the cases with and without salt

Conclusions

Phirani et al. (2009) concluded that warm water injection is necessary for the gas production from unconfined hydrate reservoirs. The vertical wells for the unconfined case are less efficient that the horizontal wells. Horizontal wells increase the area of sweep of hydrate bearing sediments leading to more production. If the wells are located in the hydrate-bearing zone, the low permeability of the region leads to a low gas production in the initial period. If the

injection well is near the aquifer layer, the convection of water becomes easy and the gas production is nonzero from the beginning. Increasing the distance between the horizontal wells decreases the amount of hydrate dissociated in the whole reservoirs and gas production decreases. The salt content increases the gas production rate a little but the production of fresh water from hydrate dissociation reduces the effect and in the case studied makes the salt effect negligible.

Future Work

In the last 6 months we have also added CO_2 as a component to the present simulator and are simulating core scale displacement of methane by CO_2.

Task 8: Seafloor and Borehole Stability:
Hugh Diagle and Brandon Dugan

We are concentrating on different scales of failure in gas hydrate systems ranging from bed-scale fracture genesis to regional-scale slope failure (Subtask 8.2). This work, which is grounded on data collected from previous hydrate studies (Subtasks 8.1 and 8.3), is not only providing constraints on what drives different types of failure, but it is also helping us characterize the controls on heterogeneous hydrate accumulations. This has led to our involvement in other hydrate collaborations with the Chevron Gulf of Mexico JIP, hydrate studies in China, and hydrate studies in Cascadia (building on Subtask 8.3 and general collaborations within DOE and outside of DOE).

Milestone Status

8.2a Link database with models – we employing 1D and 2D models for slope stability and fracture genesis based on observed and characterized properties.

8.2b Add sediment stability to models – fracture genesis models exist in 1D for dissolved-phase and free-gas phase models; slope failure models exist in 2D and are being extended to include advective flux for deep-sourced methane as initial studies suggest this is important. Presentations on these stability models are planned for the Gordon Conference on Natural Gas Hydrate in June 2010 at which time sensitivity/parameter studies based on observations. A fracture-genesis manuscript has been submitted (see update on Subtask 8.2 for details).

8.2c Conditions for (in)stability – this is ongoing work and will be completed but delayed until 06/10 as we are progressing in phases. This work will be presented at the Gordon Conference in June 2010. After establishing the conditions for slope failure, we will submit at least two manuscripts on this work – one will be discussion on the general conditions for failure; the second will be assessment of observed failures at Cascadia in collaboration with researchers at the Pacific Geoscience Centre and the University of Victoria.

Update on Subtask 8.2: Modeling (In)stability – Fracture Genesis

Fracture-hosted methane hydrate deposits exist at many sites worldwide. We estimate that thousands to millions of years are required to form fracture systems by hydraulic fracturing driven by occlusion of the pore system by hydrate. This time scale is a function of rates of fluid flow and permeability loss. Low-permeability layers in a sedimentary column can reduce this time if the permeability contrast with respect to the surrounding sediments is of order 10. Additionally we find that tensile fracturing produced by hydrate heave around hydrate lenses is a viable fracture mechanism over all but the lowermost part of

the hydrate stability zone. With our coupled fluid flow-hydrate formation model, we assess fracture formation at four well-studied hydrate provinces: Blake Ridge offshore South Carolina, Hydrate Ridge offshore Oregon, Keathley Canyon Block 151 offshore Louisiana, and the Krishna-Godavari Basin offshore India.

We simulate a one-dimensional system where methane-saturated water flows upwards. We prescribe a seafloor depth d_{sf} [m], seafloor temperature T_{sf} [K], geothermal gradient dT/dz [K m^{-1}], porosity-depth profile φ [m^3 m^{-3}], permeability-depth profile k [m^2], and vertical fluid flow rate $\vec{\mathbf{q}}_f$ [m s^{-1}]. Formation of methane hydrate is simulated by determining methane solubility for the given temperature and pressure conditions, and then performing a mass balance for water and methane. The methane solubility curve $c^l_{m,eqb}$ [kg kg^{-1}] is computed using the methodology of *Bhatnagar et al.* [2007] assuming a constant NaCl concentration of 33.5‰. We determine the hydrate saturation S_h by solving the mass balance for methane:

$$\frac{\partial}{\partial t}\left[\varphi(1-S_h)\rho_w c^l_m + \varphi S_h c^h_m \rho_h\right] - \frac{\partial}{\partial z}\left[\left|\vec{\mathbf{q}}_f\right| c^l_m \rho_w\right] = \frac{\partial}{\partial z}\left[\varphi(1-S_h) D_m \rho_w \frac{\partial c^l_m}{\partial z}\right],$$

(Equation 1)

where c^l_m and c^h_m are the concentrations of methane in the liquid and hydrate phase [kg kg^{-1}], and D_m is the diffusion coefficient for methane in water [m^2 s^{-1}]. We assume $D_m = 10^{-9}$ m^2 s^{-1} and $c^h_m = 0.134$ kg kg^{-1} [*Davie and Buffett*, 2001]. As hydrate forms, the pore space available to fluid flow is occluded. We model reduced permeability k' [m^2] as

$$k' = k(1-S_h)^2.$$

(Equation 2)

This model is based on the permeability of a series of cylindrical capillary tubes with hydrate forming a uniform coating on the walls [*Nimblett and Ruppel*, 2003], which is supported by the work of *Yun et al.* [2005] and *Lee et al.* [2007]. The pore fluid pressure P_p [Pa] in the sediments is computed from Darcy's Law:

$$P_p = \rho_w g(z + d_{sf}) + \int_0^z \frac{-\left|\vec{\mathbf{q}}\right|_f \mu}{k'} dz',$$

(Equation 3)

where μ is the viscosity of water [Pa s]. We model a constant $\vec{\mathbf{q}}_f$ and compute the pore fluid pressure profile required to maintain a constant flux as hydrate forms and permeability evolves.

We consider fracture formation by hydraulic fracturing driven by water pressure, and hydrate-induced heave. In a passive sedimentary basin, the maximum principal stress σ_1 [Pa] at a given depth z [m] is vertical and can be defined by integrating the bulk density. We assume that the total vertical stress σ_v [Pa] is equal to σ_1, and that the horizontal stress σ_h [Pa] is equal to the minimum principal stress σ_3 [Pa]. Hydraulic fractures form when the pore fluid pressure exceeds the horizontal effective stress. We define the overpressure ratio as the ratio of excess pore pressure to vertical effective stress under hydrostatic conditions:

$$\lambda^* = \frac{P_p - \rho_w g\left(d_{sf} + z\right)}{\sigma_v - \rho_w g\left(d_{sf} + z\right)} = \frac{P^*}{\sigma_v - \rho_w g\left(d_{sf} + z\right)}.$$

(Equation 4)

During normal, K_0 consolidation, the horizontal effective stress under hydrostatic conditions is typically 60% of the vertical hydrostatic effective stress [*Karig and Hou*, 1992]; for fractures to occur, the excess pore pressure P^* must exceed the horizontal effective stress - fracturing to occurs where $\lambda \geq 0.6$.

Hydrate-induced heave is a process similar to frost heave where the formation of lenses of hydrate forces sediment grains apart [*Krause*, 2000]. During growth of a hydrate lens, the solid hydrate will occupy pore space along with some fluid. The force which the hydrate lens exerts on the surrounding sediment as it grows is proportional to the volume of hydrate which can be formed from the remaining liquid volume; this concept is known as thermomolecular buoyancy and is analogous to Archimedes' Principle [*Rempel*, 2007]. The net outward force per unit area $\vec{\mathbf{F}}$ [Pa] which is exerted over the surface of the lens is given by [*Rempel et al.*, 2004; *Rempel*, 2007]

$$\vec{\mathbf{F}} = \frac{\rho_h \mathcal{L}}{T_m}\left(T_m - T_l - \int_{T_l}^{T_f} \varphi S_h dT\right)\vec{\mathbf{n}},$$

(Equation 5)

where L is the latent heat of fusion per unit mass [J kg^{-1}], T_m is the melting temperature (three-phase equilibrium temperature) of hydrate at a given depth [K], T_l is the in situ (lens) temperature [K], T_f is the temperature at the base of the MHSZ [K], S_h is the hydrate saturation

[m^3 m^{-3}], and $\vec{\mathbf{n}}$ is the outward unit normal vector. The dimensionless variable H^* = $\vec{\mathbf{F}} / \sigma_v^{'}$ represents the positive ratio of heave force to vertical effective stress. Vertical hydrate-filled fractures are thus possible when $H^* \geq 0.6$, and horizontal hydrate-filled fractures are possible when $H^* \geq 1$.

We simulated hydrate formation at four field sites: Keathley Canyon Block 151 (KC151), Blake Ridge (Site 997), Hydrate Ridge (Site 1250), and NGHP Site 10 in the Krishna-Godavari Basin offshore India. At each site we simulated a homogeneous (reference) case, with single trends of porosity and permeability with depth, and a heterogeneous case, where porosity and permeability were varied based on lithology determined from petrophysical logs. We assumed vertical flow rates of 0.4 mm yr^{-1} at KC151, 0.2 mm yr^{-1} at Blake Ridge, 300 mm yr^{-1} at Hydrate Ridge, and 35 mm yr^{-1} at NGHP Site 10. In the homogeneous cases, we found that fractures formed after 9×10^5 years at KC151, 8×10^6 years at Blake Ridge, 9000 years at Hydrate Ridge, and 10^5 years at NGHP Site 10. Fractures in all cases form first near the base of the MHSZ, where the dissolved methane concentrations are highest and initial λ^* values are largest (Figure 1). Hydrate heave is a viable fracturing mechanism over all but the lowermost few tens of meters at each site. In the heterogeneous cases, we found that fractures formed after 3×10^5 years at KC151, 8×10^6 years at Blake Ridge, 1600 years at Hydrate Ridge, and 10^5 years at NGHP Site 10. At KC151 and Blake Ridge, the location of fracture initiation was not changed from the homogeneous cases; at Hydrate Ridge and NGHP Site 10, fractures initiated at the base of some of the lower-permeability layers in the sequence (Figure 2).

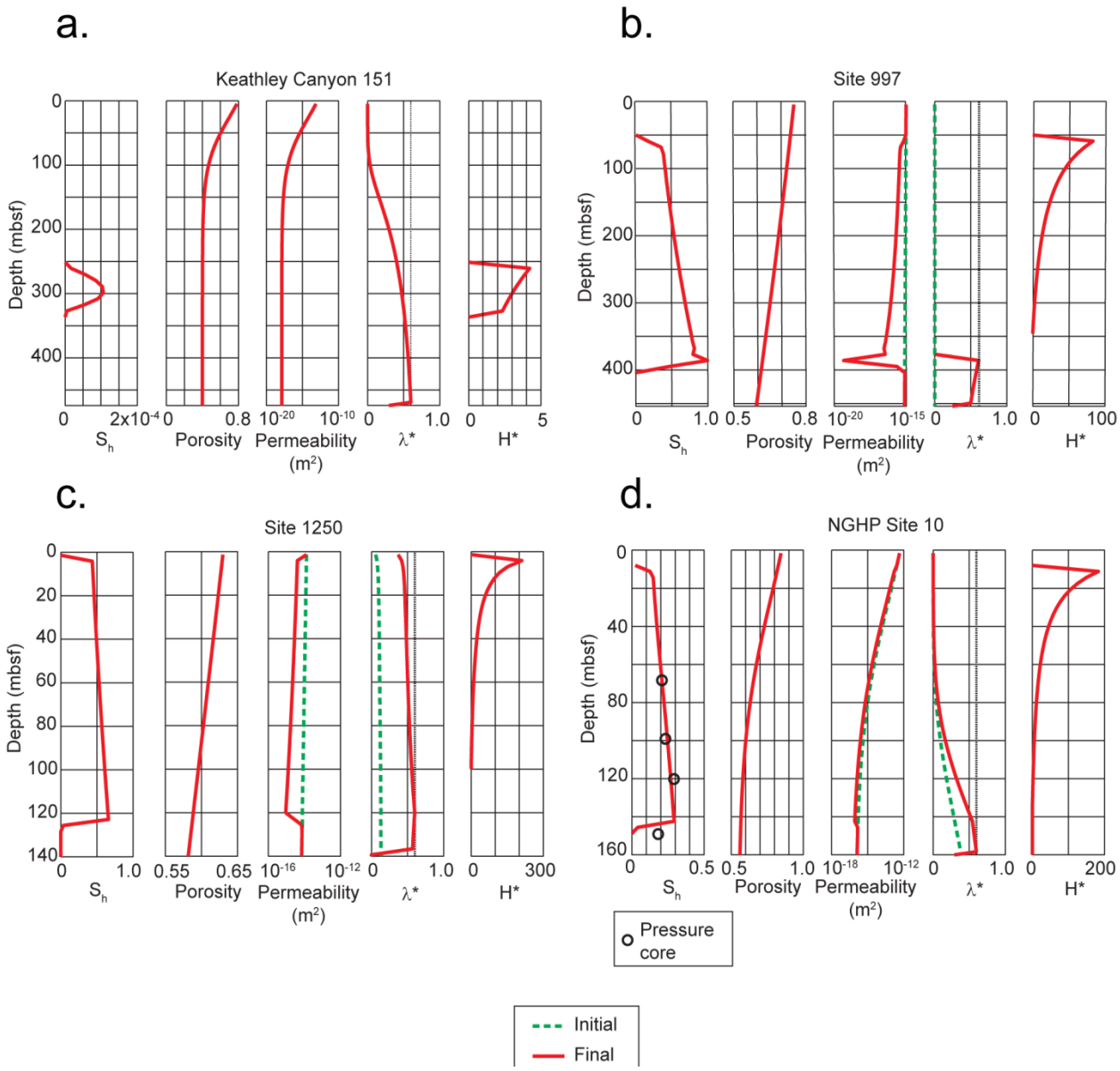

Fig. 1. (a) Model results for KC151. From left to right, hydrate saturation, porosity, permeability, overpressure ratio λ^*, and ratio of hydrate heave force to vertical effective stress H^*. The fracture criterion is represented by the dashed line at $\lambda^* = 0.6$. The hydraulic fracturing criterion is achieved after 9×10^5 years. Hydraulic fractures initiate at the base of the MHSZ. The hydrate heave force is sufficient to produce subvertical veins and fractures in the interval 250-340 mbsf. S_h is small in this case because the initial λ^* is close to the critical value of 0.6, requiring only a slight reduction in permeability to cause fracturing. (b) Model results for Blake Ridge. The fracture criterion is achieved after 8×10^6 years. Hydraulic fractures are generated first near 390 mbsf where $S_h = 0.99$. The hydrate heave force is sufficient to produce subvertical veins and fractures in the interval 50-310 mbsf. (c) Model results for Hydrate Ridge. The fracture criterion is achieved after 9×10^3 years. Fractures initiate near 122 mbsf. The hydrate heave force is sufficient to produce subvertical veins and fractures above 90 mbsf. (d) Model results for NGHP Site 10. Pressure core data are from *Lee and Collett* [2009]. The hydraulic fracturing criterion

is achieved after 10^5 years. The hydrate heave force is sufficient to produce subvertical veins and fractures in the interval 10-135 mbsf. Note how the computed S_h profile closely matches the pressure core saturations; we use this match as a constraint on vertical flow rates.

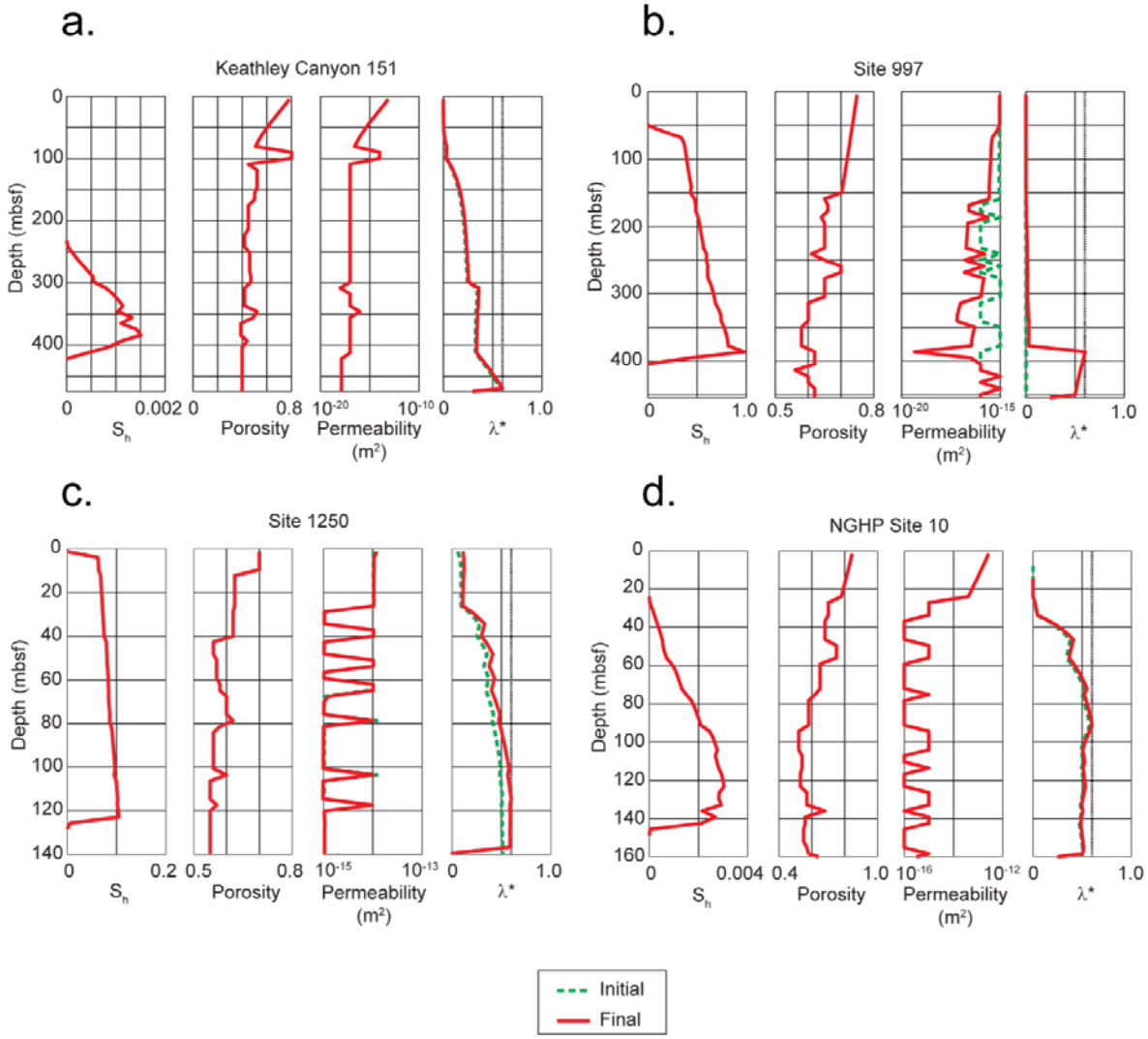

Fig. 2. (a) Model results for KC151 with heterogeneities derived from the gamma ray log. Left to right, hydrate saturation, porosity, permeability, and overpressure ratio. Porosity and permeability are derived from *Daigle and Dugan* [2009]. The fracture criterion was achieved after $3x10^5$ years. Fractures initiate at the base of the MHSZ, indicating that permeability contrasts at this site are not sufficient to cause fracturing at other depths. (b) Results for Blake Ridge with heterogeneities derived from the gamma ray log. Porosity is from ODP Leg 164 site 997; permeabilities of 10^{-15} m^2 and 10^{-16} m^2 were assigned to the silt and clay intervals. Fracture criterion was achieved after $8x10^6$ years. Fractures are predicted to initiate at 386 mbsf, which is the same location predicted for the homogeneous case (Fig. 1b). This indicates that order-of-magnitude permeability contrasts are not sufficient to change the location of fracture initiation at this site. (c) Results for Hydrate Ridge with heterogeneities derived from the gamma ray log. Porosity is from ODP Leg 204 site 1250. Permeabilities of 10^{-14} m^2 and 10^{-15} m^2 were assigned to the silt and clay intervals [*Tan et al.*, 2006]. Fracture criterion was achieved after 1600

years. Fractures initiate at the base of the MHSZ and at the base of a low-permeability layer near 115 mbsf illustrationg how low-permeability layers can cause fracturing throughout the MHSZ at lower S_h and in less time than in homogeneous cases provided flow rates are high enough.(d) Results for NGHP Site 10 with lithologic heterogeneities derived from the gamma ray log. Porosity is taken from the bulk density log; permeabilities of 10^{-15} m^2 and 10^{-16} m^2 were assigned to the silt and clay intervals, respectively. The fracture criterion is achieved after $6x10^3$ years. Fractures initiate at the base of a clay layer at 87 mbsf.

Fractures will tend to initiate first in locations which have high initial λ^* values. Initial λ^* values are determined by permeability and fluid flux, and will be higher in areas with low permeability and/or high flux. In the case of KC151 and Blake Ridge, the fluid fluxes are so low that lithologic heterogeneities are not sufficient to cause fractures to nucleate in locations other than the base of the MHSZ. Hydrate Ridge and NGHP Site 10 represent the other endmember, where the combination of high fluxes and low-permeability layers is sufficient to cause fracture initiation in the low-permeability layers. Hydrate heave is more likely to be a significant fracturing mechanism at low-flux sites like KC151 or Blake Ridge.

We are now extending this work by investigating the effect of free gas within the MHSZ on fluid pressures. To accomplish this, we have developed a model which couples a chloride mass balance relation with hydrate and free gas stability conditions. As hydrate forms, salts are excluded from the water which is incorporated into the hydrate crystals. This has the effect of increasing the salinity in the remaining pore fluid [e.g., *Liu and Flemings*, 2006]. The increased salinity in the pore fluid causes a depression of the liquid+hydrate+free gas triple point [*Sloan*, 1990], and it is possible to increase salinity within the MHSZ to the point where free gas is stable along with dissolved methane and hydrate.

We solve the mass balance equation for methane dissolved in pore fluid and methane in free gas:

$$\frac{\partial}{\partial t}\left[\varphi\left(1-S_h-S_g\right)\rho_w c_m^l+\varphi S_h c_m^h \rho_h+\varphi S_g c_m^g \rho_g\right]-\frac{\partial}{\partial z}\left[\left|\vec{\mathbf{q}}_f\right| c_m^l \rho_w+\left|\vec{\mathbf{q}}\right|_g c_m^g \rho_g\right]=$$

$$\frac{\partial}{\partial z}\left[\varphi\left(1-S_h-S_g\right)D_m \rho_w \frac{\partial c_m^l}{\partial z}\right] \quad ,$$

(Equation 6)

where S_g is the fraction of pore space occupied by free gas [m^3 m^{-3}], c_m^g is the mass fraction of free gas composed of methane [kg kg^{-1}] (assumed to be 1), ρ_g is the gas density computed from the ideal gas law [kg m^{-3}], and $\vec{\mathbf{q}}_g$ is the gas flux [m s^{-1}]. We assume a constant pressure at the base of the domain rather than a constant flux as before. Fluxes are computed from Darcy's law:

$$\vec{\mathbf{q}}_i = -\frac{kk_{ri}}{\mu_i}\left(\frac{dP_i}{dz} - \rho_i \vec{\mathbf{g}}\right),$$

(Equation 7)

where $\vec{\mathbf{q}}_i$, P_i, ρ_i, and μ_i are the flux, pressure, density, and viscosity of component *i*, and k_{ri} is the relative permeability for component *i*. Gas viscosity is calculated from the Lennard-Jones potential [*Bird et al.*, 2007]. Relative permeabilities are calculated using Corey's model [*Bear*, 1972]. The difference between the gas phase pressure and the water pressure is the capillary pressure, which we compute using a J-function [*Bear*, 1972] based on mercury injection capillary pressure measurements on a marine mudstone.

Our preliminary results for Hydrate Ridge indicate that free gas does not significantly alter the time required to achieve the fracture criterion, and that lithologic heterogeneities have the same effect as before, namely reducing the time to fracture and causing fractures to nucleate in low-permeability layers. We ran simulations to reach a fracture criterion where the gas phase pressure equals the vertical effective stress; in the homogeneous case, the simulation took 6018 years (Figure 3), and in the heterogeneous case, the simulation took 2262 years (Figure 4).

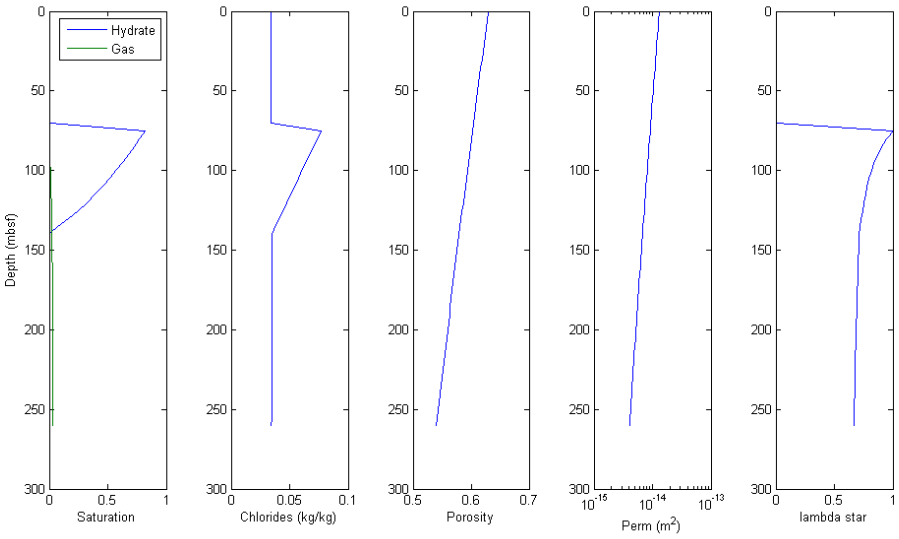

Fig. 3. Model results for Hydrate Ridge with free gas in the MHSZ with homogeneous lithology. Simulation took 6018 years to achieve the fracture criterion. Left to right, saturations, chloride mass fraction, porosity, permeability, and λ^*. Fractures nucleate near 70 mbsf where the hydrate saturation is near 80%.

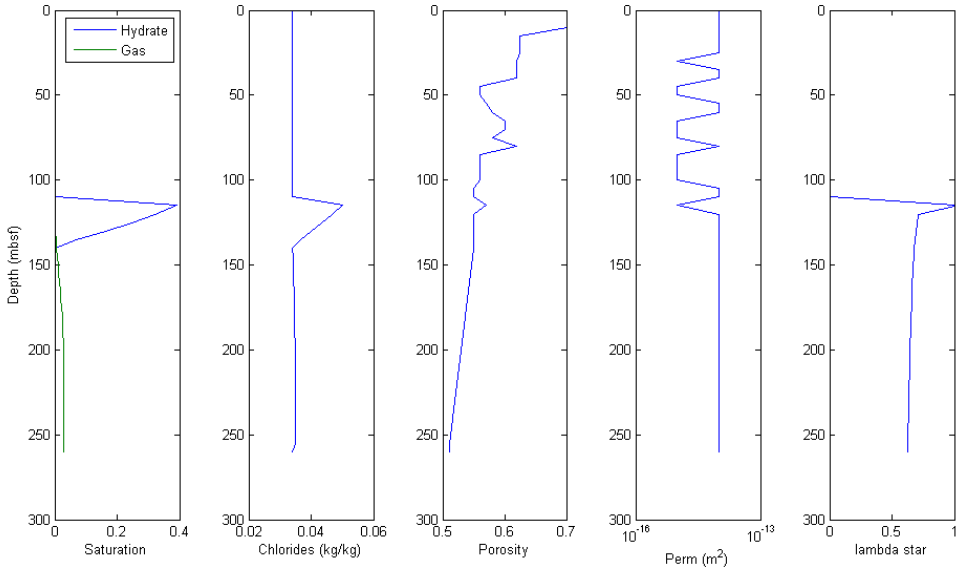

Fig. 4. Model results for Hydrate Ridge with free gas in the MHSZ and heterogeneous lithology. Simulation took 2262 years to achieve the fracture criterion. Hydrate saturation at fracture is less than in Figure 3, and fracture initiate in the low-permeability layer near 120 mbsf.

These models have also allowed us to study preferential hydrate accumulation in higher-permeability layers. Observations from Hydrate Ridge [*Su et al.*, 2006; *Weinberger & Brown*, 2006] and the northern Cascadia margin [*Malinverno et al*., 2008; *Torres et al*., 2008] indicate that hydrates in these areas are located preferentially in layers with larger grains and higher permeability. Recent experimental data suggest that the triple point is depressed in sediments with small pore throats because of capillary effects [*Henry et al.*, 1999; *Uchida et al*., 2004; *Torres et al*., 2008]. This has the effect of increasing the solubility of methane in these sediments, so that higher concentrations of dissolved methane are required to form methane in lower-permeability layers than in higher-permeability layers. *Malinverno* [2010] modeled hydrate formation in an interbedded silt-clay sequence from methane produced in situ by biogenic processes, and found that the higher solubility in the clay layers produced a relative oversaturation in these layers relative to the silts, resulting in a diffusive flux of methane from the clays to the silts. This diffusive flux was found to be sufficient to produce the observed hydrate distributions from IODP311 Site U1325. However, this location is interpreted to be an advective methane system based on porewater chlorinity observations [*Riedel et al.*, 2006]. We are interested in determining if similar hydrate saturation profiles can be obtained by advective transport of methane.

Our preliminary modeling results indicate that advective methane transport can result in preferential hydrate formation in silts relative to clay because of the higher solubility of methane in the clays. We modeled flow through a 50 m-thick

domain of alternating 10 m-thick layers of silt and clay. Temperature, pressure, permeability, and porosity conditions were based on Hydrate Ridge Site 1250; we assumed permeabilities of 10^{-15} m^2 in the clays and 10^{-14} m^2 in the silts. Solubility was computed by increasing the triple point temperature T_{3P} by an increment $\Delta T_{3P} = (0.0016 - 0.23/d)T_{3P}$, where d is the pore diameter in nanometers [*Uchida et al*., 2004; *Torres et al*., 2008]. Hydrate forms near the tops of the clay layers and throughout the silt layers; fractures propagate upwards through the clay layers but not in the silt layers. After ~60,000 years of simulation time, fractures propagate through the lower two clay layers, bypassing the intervening silt layer (Figure 5). We plan to model the turbidite sequence encountered in IODP 311 and modeled by *Malinverno* [2010] once we find suitable permeability and fluid flow constraints.

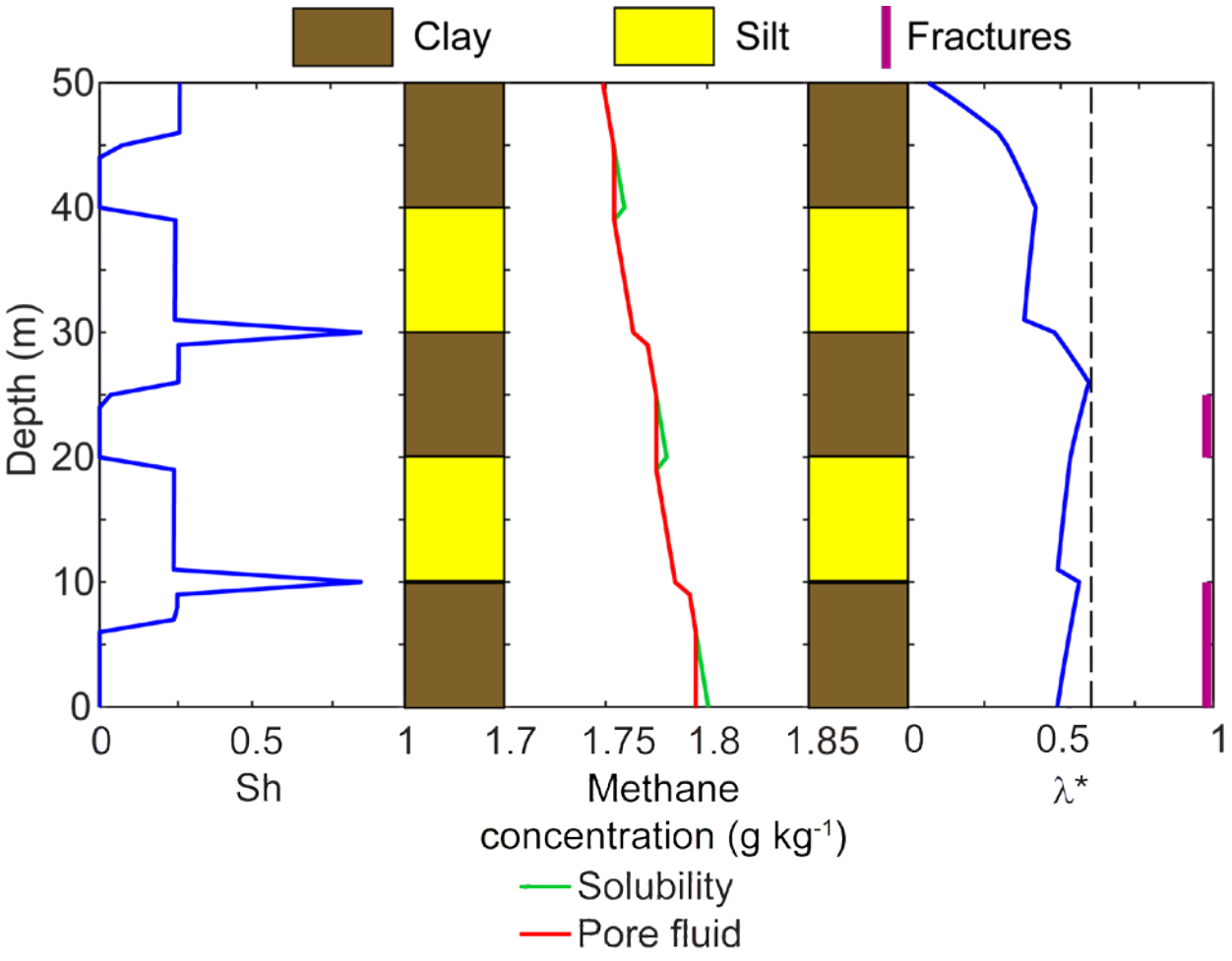

Fig. 5. Model results for flow through interbedded silts and clays with capillary effects on solubility. Left to right, hydrate saturation, solubility and concentration of methane in pore fluid, overpressure ratio. Lithology column is indicated between tracks in yellow and brown. Fractures shown on the far right as purple bars. After 60,000 years, fractures have propagated upwards through the lowermost clay and partway through the next clay, but have bypassed the intervening silt. Hydrate forms preferentially in the silts and near the top of the clay layers.

References

Bear, J. (1972), *Dynamics of Fluids in Porous Media*, 784 pp, Dover, Mineola, New York.

Bhatnagar, G., Chapman, W.G., Dickens, G.R., Dugan, B., and G.J. Hirasaki (2007), Generalization of gas hydrate distribution and saturation in marine sediments by scaling of thermodynamic and transport processes, *Am. J. Sci., 307*, 861-900, doi:10.2475/06.2007.01.

Bird, R.B., Stewart, W.E., Lightfoot, E.N. (2007), *Transport Phenomena* (2nd Ed.), 905 pp, John Wiley & Sons, New York.

Daigle, H., and B. Dugan (2009), Extending NMR data for permeability estimation in fine-grained sediments, *Mar. Petrol. Geol.*, *26*(8), 1419-1427, doi:10.1016/j.marpetgeo.2009.02.008.

Davie, M.K., and B.A. Buffett (2001), A numerical model for the formation of gas hydrate below the seafloor, *J. Geophys. Res., 106*(B1), 497-514.

Henry, P., Thomas, M., and M.B. Clennell (1999), Formation of natural gas hydrates in marine sediments 2. Thermodynamic calculations of stability conditions in porous sediments, *J. Geophys. Res.*, *104*(B10), 23005-23022.

Karig, D.E., and G. Hou (1992), High-stress consolidation experiments and their geologic implications, *J. Geophys. Res.*, *97*(B1), 289-300.

Krause, F.F. (2000), Genesis and geometry of the Meiklejohn Peak lime mud-mound, Bare Mountain Quadrangle, Nevada, USA: Ordovician limestone with submarine frost heave structures – a possible response to gas clathrate hydrate evolution, *Sed. Geol.*, *145*, 189-213.

Lee, J.Y., Yun, T.S., Santamarina, J.C., and C. Ruppel (2007), Observations related to tetrahydrofuran and methane hydrates for laboratory studies of hydrate-bearing sediments, *Geochem. Geophys. Geosyst.*, *8*(6), Q06003, doi:10.1029/2006GC001531.

Lee., M.W., and T.S. Collett (2009), Gas hydrate saturations estimated from fractured reservoir at Site NGHP-01-10, Krishna-Godavari Basin, India, *J. Geophys. Res.*, *114*, B07102, doi:10.1029/2008JB006237.

Liu, X., Flemings, P.B., 2006. Passing gas through the hydrate stability zone at southern Hydrate Ridge, offshore Oregon. *Earth Planet. Sci. Lett., 241*, 211-226, doi:10.1016/j.epsl.2005.10.026.

Malinverno, A. (2010), Marine gas hydrates in thin sand layers that soak up microbial methane, *Earth Planet. Sci. Lett., 292*, 399-408, doi:10.1016/j.epsl.2010.02.008.

Malinverno, A., Kastner, M., Torres, M.E., Wortmann, U.G. (2008), Gas hydrate occurrence from pore water chlorinity and downhole logs in a transect

across the northern Cascadia margin (Integrated Ocean Drilling Program Expedition 311), *J. Geophys. Res., 113*, B08103, doi:10.1029/2008JB005702.

Nimblett, J., and C. Ruppel (2003), Permeability evolution during the formation of gas hydrates in marine sediments, *J. Geophys. Res., 108*(B9), doi:10.1029/2001JB001650.

Rempel, A.W. (2007), Formation of ice lenses and frost heave, *J. Geophys. Res., 112*, F02S21, doi:10.1029/2006JF000525.

Rempel, A.W., Wettlaufer, J.S., and M.G. Worster (2004), Premelting dynamics in a continuum model of frost heave, *J. Fluid Mech.*, *498*, 227-244, doi:10.1017/S0022112003006761.

Riedel, M., Collett, T.S., Malone, M.J., Expedition 311 Scientists (2006), *Proc. IODP, 311*, Integrated Ocean Drilling Program, Washington, DC, doi:10.2204/iodp.proc.311.2006.

Sloan, E.D. Jr. (1990), *Clathrate Hydrates of Natural Gases*, 641 pp., M. Dekker, New York.

Su, X., Song, C.-B., Fang, N.-Q. (2006), Relationship between sediment granulometry and the presence of gas hydrate on Hydrate Ridge, edited by A.M. Tréhu et al., *Proc. Ocean Drill. Program Sci. Results*, *204*, 1-30, doi:10.2973/odp.proc.sr.204.115.2006.

Tan, B., Germaine, J.T., and P.B. Flemings (2006), Data report: Consolidation and strength characteristics of sediments from ODP Site 1244, Hydrate Ridge, Cascadia continental margin, edited by A.M. Tréhu et al., *Proc. Ocean Drill. Program Sci. Results*, *204*, 1-148, doi:10.2973/odp.proc.sr.204.102.2006.

Torres, M.E., Tréhu, A.M., Cespedes, N., Kastner, M., Wortmann, U.G., Kim, J.-H., Long, P., Malinverno, A., Pohlman, J.W., Riedel, M., Collett, T. (2008), Methane hydrate formation in turbidate sediments of northern Cascadia, IODP Expedition 311, *Earth Planet. Sci. Lett., 271*, 170-180, doi:10.1016/j.epsl.2008.03.061.

Uchida, T., Nagao, J., Yakushev, V.S., Istomin, V.A., Minagawa, H., Ebinuma, T., Narita, H., Takeya, S., Chuvilin, E.M., Ohmura, R. (2004), Decomposition of methane hydrates in sand, sandstone, clays and glass beads, *J. Geophys. Res., 109,* B05206, doi:10.1029/2003JB002771.

Weinberger, J.L., Brown, K.M. (2006), Fracture networks and hydrate distribution at Hydrate Ridge, Oregon, *Earth Planet. Sci. Lett., 245*, 123-136, doi:10.1016/j.epsl.2006.03.012.

Yun, T.S., Francisca, F.M., Santamarina, J.C., and C. Ruppel (2005), Compressional and shear wave velocities in uncemented sediment containing gas hydrate, *Geophys. Res. Lett.*, *32*, L10609, doi:10.1029/2005GL022607.

Task 9: Geophysical Imaging of Gas Hydrate and Free Gas Accumulations
P. Jaiswal and C.A. Zelt
Report will be issued with end of Phase 4 report.

Task 10 Technology Transfer

Publications

Manuscript

Elevated Ocean Bottom Water Temperature and Abundant Marine Gas Hydrate in the Early Palaeogene. Guangsheng Gu, Gerald R. Dickens*, Gaurav Bhatnagar, Frederick S. Colwell, George J. Hirasaki, Walter Chapman. In Review and Revision.

Daigle, H., Dugan, B., in review, Origin and evolution of fracture-hosted methane hydrate deposits, Journal of Geophysical Research.

Waite, W.F, C. Santamarina, D. Cortes, B. Dugan, N. Espinoza, J. Germaine, J. Jang, J. Jung, T. Kneafsey, H. Shin, K. Soga, W. Winters, T-S. Yun, accepted pending revision, Physical properties of hydrate-bearing sediments, Reviews of Geophysics, 47, RG4003, doi:10.1029/2008RG000279.

Journal articles (draft manuscript) - Prepared the first draft for our manuscripts

1. *"Pore water chemistry profiles across SMT above marine gas hydrates systems: A numerical modeling perspective*" to be submitted to *Journal of Geophysical Research* (Chatterjee et al.)

2. *"Analytical theory for relating depth of the sulfate-methane transition to gas hydrate saturation*" to be submitted to *Geochemistry, Geophysics, Geosystems* (Bhatnagar et al.)

Conference presentations

S. Chatterjee, G. Bhatnagar, W. G. Chapman, G. R. Dickens, B. Dugan, G. J. Hirasaki, "*Sulfate, Alkalinity, Calcium and Carbon isotope* $\delta^{13}C$ *profiles as an indicator of upward methane flux*", (oral presentation) American Geophysical Union (AGU) Fall meeting, San Francisco, CA, December 2009

S. Chatterjee, G. Bhatnagar, W. G. Chapman, B. Dugan, G. R. Dickens, G. J. Hirasaki, "*Carbon cycling across sulfate-methane transition above marine gas hydrate systems*", (oral presentation) Society of Petroleum Engineers (SPE) Gulf-coast regional student paper contest, Lubbock, TX, April 2010

S. Chatterjee, G. Bhatnagar, W. G. Chapman, B. Dugan, G. R. Dickens, G. J. Hirasaki, "*Sulfate-Methane Transition depth as a proxy for methane flux above gas hydrate systems*", (selected for poster presentation) Gordon Research Conference – Natural gas hydrate systems, Waterville, ME, June 2010

Daigle, H., Dugan, B., 2009, Fracture genesis in methane hydrate systems, Rice University Department of Earth Science seminar, Houston, TX (17 November 2009).

Daigle, H., Dugan, B., 2009, Fracture genesis and fracture filling in methane hydrate systems, American Geophysical Union Fall Meeting, San Francisco, CA (17 December 2009).

Daigle, H., Dugan, B., 2010, Origins of fracture-hosted methane hydrates, Chevron technology talk, Houston, TX (11 March 2010).

DOE methane hydrate meeting, Georgia Tech University, Atlanta, GA

1. *Carbon cycling across SMT above marine gas hydrates systems: A numerical modeling perspective* – Monday Jan 25, 2010

2. *Effect of lithologic heterogeneity on gas hydrate distribution* – Wednesday Jan 27, 2010

3. Effect of Hydrocarbon Components on Hydrate/Gas Distribution and BSR. Guangsheng Gu, Walter Chapman, Priyank Jaiswal, George J. Hirasaki, DOE Hydrate Meeting, 2010 Jan 25-29, Atlanta, GA.

Daigle, H., 2009, Fracture genesis and fracture filling in methane hydrate systems, DOE/NETL Methane Hydrate Workshop, Atlanta, GA (26 January 2010).

Dugan, B., 2010, Physical properties studies: flow, fractures, and failures, DOE/NETL Methane Hydrate Workshop, Atlanta, GA (26 January 2010).

Hydrate Collaborations and Community Service

Dugan was a member of the panel discussion on Gas Hydrates and Slope Stability at the Submarine Mass Movements and Their Consequences Symposium, Austin, TX, November 7-12, 2009.

Dugan has opened hydrate-related collaborations with M. Riedel (Pacific Geoscience Center, British Columbia, Canada) and N. Scholz (University of Victoria, British Columbia, Canada) to model the hydrate formation and slope failure along the Cascadia margin and with Xiujuan Wang (Institute of Oceanology, Chinese Academy of Sciences) to study flow systems related to

heterogeneous hydrate accumulations in the South China Sea and to compare them with the Gulf of Mexico.

Dugan has also been collaborating with the Chevron Gulf of Mexico JIP team to develop the science plan for Leg III in 2011. Dugan is leading the physical properties science plan initiative that will be integrated with the overall science plan to meet the objectives of the JIP in 2011.

Cost Plan / Status

The Cost Plan / Status will updated with the End of Phase 4 report.

Milestone Plan/Status

Task	Milestone: Status and Results	Date	Status
5. Carbon inputs and outputs to gas hydrate systems	5.1a Measure iodine in sediments We have measured iodine concentrations in pore waters and sediments from 4 gas hydrate systems.	12/07	Done (except writing)
	5.1b Constrain C_{org} inputs from iodine We have measured the content and isotopic composition of organic carbon and carbonate in sediment from cores of several gas hydrate systems. We are beginning to incorporate the results into models.	10/08	Partly Done
	5.2a Construct metal profiles in sediments We have measured metal contents in pore water and sediment from cores of two gas hydrate systems along the Peru Margin and in the Sea of Japan. The Sea of Japan work has been published (Snyder et al., 2007).	12/09	Done (except writing)
	5.2b Modeling/integrating profiles We are beginning to incorporate the results into models. We have written an article defending our use of the SMT as a proxy for methane loss through AOM.	12/10	Begun

6. Numerical models for quantification of hydrate and free gas accumulations	6.1 Model development. The recipient shall develop finite difference models for the accumulation of gas hydrate and free gas in natural sediment sequences on geologically relevant time scales.	9/07	done
	6.2: Conditions for existence of gas hydrate The recipient shall summarize, quantitatively, the conditions for the absence, presence, and distribution of gas hydrates and free gas in 1-D systems by expressing the conditions in terms of dimensionless groups that combine thermodynamic, biological and lithologic transformation, and transport parameters.	3/07	done

	6.3 Compositional effect on BSR The recipient shall add to the numerical model, developed under this task, a chloride balance and multi-hydrocarbon capability specifically to investigate how hydrocarbon fractionation might affect Bottom Simulating Reflectors (BSRs).	7/07	Partialy done
	6.4: Amplitude Attenuation and chaotic zones due to hydrate distribution The recipient shall simulate preferential formation of gas hydrate in coarse-grained, porous sediment in 2-D by linking fluid flux to the permeability distribution.	3/09	started
	6.5: Processes leading to overpressure The recipient shall quantify, by simulation and summarize by combination of responsible dimensionless groups, the conditions leading to overpressure to the point of sediment failure.	3/08	Collaborating with task 8
	6.6 Concentrated hydrate and free gas The recipient shall, using 2-D and 3-D models, simulate lateral migration and concentration of gas hydrate and free gas in structural and stratigraphic traps.	3/08	ongoing
	6.7 Focused free gas, heat and salinity The recipient shall quantify, using 2-D and 3-D model simulations and comparisons to available observations, the factors controlling the process of localized upward migration of free gas along faults and lateral transfer to dipping strata that can lead to chaotic zones and possible accumulations of concentrated hydrate.	9/09	started
	6.8 Sulfate profile as indicator of methane flux The recipient shall compute, for systems where data on the sulfate profile is available, the oxidation of methane by sulfate and shall indicate the perceived level of effect on gas hydrate accumulation and the data's value as an indicator of methane flux.	7/07	Done, drafting manuscript.
	6.9 Application of models to interpretation of case studies. The models developed in Task 6 will be applied to case studies in the interpretation of each of the other tasks.	6/10	started
7. Analysis of production strategy	7.1a Pore scale model development and Hydrate code comparison For this milestone, we will develop pore-scale models of hydrate accumulation by simulation. Our hydrate code will be used to solve a set of problems formulated by the Code Comparison Study group. Our results will be	1/08	6/08 This task is complete

	compared with those of other hydrate codes. Should be changed to: 6/08 Reason: The starting date was moved to 6/07 Status: Code comparison study is 100% complete.		
	7.1b Petrophysical and thermophysical properties of hydrate sediments from pore-scale model For this milestone, we will assume the pore-scale models of hydrate accumulation developed in the last milestone and estimate transport properties as a function of hydrate and gas saturations. Should be changed to: 6/09 Reason: The starting date was moved to 6/07	1/09	6/09 This task is complete
	7.2a Modeling of several production strategies to recover gas from marine hydrates Several production strategies would be modelled using the transport property correlations developed in the previous milestone. Optimal strategies will be identified. Should be changed to: 6/10	1/10	In progress
	7.2b Effect of marine reservoir heterogeneities on production of methane Reservoir heterogeneity anticipated in marine environments (known or determined through other tasks) would be incorporated. Appropriate hydrate distributions, either constrained from experimental data or mechanistic simulations (Task 5) would be used. Sensitivity of gas production to the heterogeneities would be calculated. Should be changed to: 6/11 Reason: The starting date was moved to 6/07 Status: Have not started	12/10	This task will start in 6/10
8. Seafloor and borehole stability	8.1a Collection of data We have collected the published data and are working it into a data base. We are also working on a review paper summarizing the state of the art settings. This will include laboratory experiments, field data, published results, and unpublished data.	05/08	Completed
	8.1c Complete database We are organizing the data from task 8.1a into a format that can be searched and used by researchers trying to understand mechanical behavior of hydrate-bearing sediment. We will also identify key gaps in the database for focusing future hydrate research endeavors. We have started exchanging these data with the modeling components of this project.	10/09	On target

	8.2a Link database with models We have started passing data along to the modeling groups so they can use sediment properties from hydrate provinces as they simulate hydrate accumulation and production.	08/08	On target
	8.2b Add sediment stability to models Standard stability calculations have been implemented in a standard basin model. Now that it is functional we will work with the hydrate accumulation model to add a stability calculation to the 2-D models.	10/08	On target
	8.2c Conditions for (in)stability After implementing the stability model in the hydrate accumulation code, we can explore the conditions (e.g., hydrate dissociation, sea-level fall) that could drive slope failure and hydrate/methane release or lead to borehole failures during production.	9/09	On target
9 Geophysical imaging of hydrate and free gas	9.1 Preliminary processing and inversion of seismic data. Perform conventional seismic reflection processing, velocity analysis, travel time tomography, and other analyses as deemed appropriate and necessary.	8/08	Done (except writing)
	9.2: Final 1-D elastic and 2-D acoustic waveform inversion. Apply 1-D elastic and 2D acoustic inversions on data obtained from subtask 9.1 to derive determine high-resolution elastic and acoustic properties.	8/09	Delayed due to lab development
	9.3: Rock physics modeling. Apply rock physics models to the developed seismic models to estimate hydrate saturation and lithology through application of well log data in conjunction with data from subtask 9.2. For this subtask we shall seek to collaborate with research being conducted under separately funded DOE-NETL projects (DE-FC26-05NT42663 with Stanford University, "Seismic-Scale Rock Physics of Methane Hydrate" and others as applicable).	8/10	On Target

National Energy Technology Laboratory

626 Cochrans Mill Road
P.O. Box 10940
Pittsburgh, PA 15236-0940

3610 Collins Ferry Road
P.O. Box 880
Morgantown, WV 26507-0880

One West Third Street, Suite 1400
Tulsa, OK 74103-3519

1450 Queen Avenue SW
Albany, OR 97321-2198

539 Duckering Bldg./UAF Campus
P.O. Box 750172
Fairbanks, AK 99775-0172

Visit the NETL website at:
www.netl.doe.gov

Customer Service:
1-800-553-7681